remote sensing

MDPI

Article

Validation of Satellite Sea Surface Temperature in the Coastal Agulhas Current System Using USV Observations

Neha Ramsarup [1,2,*], Tamaryn Morris [1], Juliet Hermes [1,2,3], Sebastiaan Swart [2,4] and Marcel Du Plessis [4]

[1] South African Environmental Observation Network, Egagasini Node, Cape Town 8021, South Africa; t.morris@saeon.nrf.ac.za (T.M.); jc.hermes@saeon.nrf.ac.za (J.H.)
[2] Department of Oceanography, University of Cape Town, Cape Town 7701, South Africa; sebastiaan.swart@marine.gu.se
[3] Institute for Coastal and Marine Research, Ocean Sciences Campus, Nelson Mandela University, Gqeberha 6031, South Africa
[4] Department of Marine Sciences, University of Gothenburg, 40530 Göteborg, Sweden; marcel.du.plessis@gu.se
* Correspondence: rmsneh002@myuct.ac.za

Highlights

What are the main findings?

- Satellite SST accuracy varied strongly with oceanographic regime, with reduced performance during rapid coastal upwelling.
- Sentinel-3 best captured SST variability, while OSTIA provided reliable gap-free fields and MUR showed the largest errors.

What are the implications of the main findings?

- Optimal satellite product choice depends on oceanographic conditions and application needs.
- Combining satellite and autonomous in situ observations helps resolve sub-daily coastal variability.

Abstract

Satellite sea surface temperature (SST) products are used to monitor coastal ocean variability, yet their performance in dynamic boundary current systems remains uncertain. This study evaluates infrared (Sentinel-3, MODIS and VIIRS) and blended (OSTIA and MUR) SST product performance using high-resolution in situ observations from a Sailbuoy autonomous surface vehicle deployed along the southeastern Agulhas Current coastal region. Satellite products were collocated with Sailbuoy SST observations across two contrasting surveys, representing moderate shelf-break variability in May–June 2024 and a rapidly evolving coastal upwelling event in February–March 2025. Standard statistical metrics and sensitivity analyses assessed product performance under differing oceanographic conditions. All products showed significant agreement with Sailbuoy observations during 2024 ($r = 0.84$–0.94; $p < 0.01$), but performance deteriorated during the 2025 upwelling event. Sentinel-3 demonstrated the most robust overall performance, followed by OSTIA, whereas MUR exhibited the largest errors and strongest attenuation of SST variability (RMSE = 2.23 °C). Performance differences were associated with rapid cooling, strong thermal gradients, cloud-induced sampling limitations, and differences in product processing. These findings demonstrate that satellite SST performance depends strongly on the oceanographic regime and highlight the importance of accounting for sub-daily variability and sensor-specific sampling when validating SST products in dynamic coastal environments.

Check for updates

Academic Editor: Kun Shi

Received: 23 September 2026
Revised: 27 October 2026
Accepted: 3 November 2026
Published: 25 November 2026

Copyright: © 2026 by the authors. Licensee MDPI, Basel, Switzerland. This article is an open access article distributed under the terms and conditions of the Creative Commons Attribution (CC BY) license.

Keywords: sea surface temperature; satellite remote sensing; SST validation; Sailbuoy; Agulhas Current coastal system; coastal upwelling; coastal monitoring

1. Introduction

Sea surface temperature (SST) is a fundamental variable of the Earth's climate system, governing the exchange of heat, momentum, moisture, and gases across the air–sea interface [1,2]. By regulating global heat distribution and modulating atmospheric circulation, SST acts as a key coupling variable between the ocean and atmosphere. This role is particularly important given that the ocean stores more than 90% of excess heat within the global climate system [3–5]. Beyond its role in physical climate processes, SST is a primary driver of marine ecosystem structure and function. Surface temperature variability influences primary productivity, species distribution, and biogeochemical cycling in coastal regions where nutrient availability is closely linked to upper-ocean dynamics [6,7]. Consequently, accurate and spatially resolved SST observations are essential for understanding ocean and ecosystem variability, particularly in dynamic coastal environments [3].

Resolving SST variability and its spatial gradients is essential for characterising coastal processes and fine-scale ocean dynamics [8]. Much of this variability is driven by mesoscale and submesoscale features, including fronts, eddies, and meanders, which generate pronounced spatial and temporal variations in SST [9,10]. Through their association with localised upwelling and downwelling, these features play a central role in shaping both the physical and biological structure of the ocean [11,12]. However, capturing this variability across the full range of spatial and temporal scales remains a major observational challenge [13,14]. Historically, SST observations were limited to in situ platforms such as ships-of-opportunity, drifting buoys, and moored arrays [15]. While these measurements are highly accurate, they are spatially and temporally sparse, leaving large regions of the global ocean under-sampled [3]. The development of satellite remote sensing has transformed ocean observation by providing synoptic, near-global coverage of SST at high spatial and temporal resolution [1,16,17]. Modern sensors now provide observations at spatial resolutions of 1 km, enabling the detection of mesoscale and submesoscale features [18,19]. Combined with regular sampling and broad spatial coverage, these capabilities make satellite observations well suited for monitoring SST variability across multiple scales [20].

Despite these advances, satellite SST retrievals are subject to several sources of uncertainty. Infrared sensors measure thermal emission from the ocean surface and provide high spatial resolution observations, but are strongly limited by cloud cover, resulting in data gaps in persistently cloudy regions [1,21]. These measurements also require atmospheric corrections for absorption and emission by water vapour, aerosols, and greenhouse gases, which can introduce uncertainty. The high concentration of water vapour in humid marine environments can attenuate the infrared signal, leading to a negative bias in SST if not properly accounted for [1,22,23]. In contrast, microwave radiometers provide almost all-weather coverage by penetrating non-precipitating cloud [17,24], but at much coarser spatial resolutions (~25 km), limiting their ability to resolve fine-scale features [25]. To mitigate these limitations, many modern SST products combine infrared and microwave observations and apply interpolation and optimal estimation techniques to produce gap-free fields [26]. However, these approaches introduce additional smoothing, meaning the effective resolution of analysed SST fields is often coarser (~5 km) than the nominal grid resolution [27,28], potentially obscuring fine-scale variability.

As a result, the performance of satellite SST products remains uncertain in dynamically complex regions, making validation essential for quantifying errors and assessing product

suitability for scientific and operational applications [25,29]. This is particularly important in coastal western boundary current systems, where land contamination, persistent cloud cover, and strong horizontal gradients can degrade satellite retrieval accuracy [30,31]. Long-term analyses combining satellite observations with in situ SST records can help characterise temperature variability and assess satellite-product biases in coastal transition zones, where observational coverage remains challenging [32]. Although conventional observing platforms, including drifting buoys and Argo floats, provide valuable measurements across diverse oceanographic environments [33], their sampling characteristics may limit the availability of sustained, high-frequency observations along specific coastal transects or across rapidly evolving oceanographic features [34,35]. In highly dynamic coastal environments, strong spatial and temporal SST variability can further complicate satellite-in situ comparisons [9]. Evaluating satellite SST products under these conditions is therefore important for understanding their capabilities and limitations in complex oceanographic systems such as the Agulhas Current.

The Agulhas Current system is one of the most energetic western boundary current regions globally and presents a challenge for satellite-derived SST products. Flowing southward along the east coast of South Africa, it transports warm Indian Ocean water toward the Southern Ocean and forms an integral part of the global thermohaline circulation [11]. The current is characterised by intense velocity cores (exceeding 2 m s^{-1}), strong thermal gradients, and frequent mesoscale variability, including eddies and shear instabilities [36–38]. Interactions with the continental shelf and coastal bathymetry generate filaments, warm intrusions, and sharp thermal fronts, influencing coastal regions such as Algoa Bay [39]. These dynamics are further complicated by coastal upwelling driven by wind-induced Ekman transport, which introduces cold, nutrient-rich water into the upper ocean [39]. The coexistence of the warm Agulhas Current (up to 26 °C) and cooler upwelled water (as low as 14 °C) produces a highly heterogeneous thermal environment that challenges the ability of satellite products to resolve fine-scale structure and increases sensitivity to smoothing and interpolation effects [18]. Persistent cloud cover and high atmospheric water vapour further degrade retrieval accuracy, while the lack of high-resolution in situ observations limits the ability to robustly validate satellite-derived SST in this region [40]. Reported biases of up to 6 °C between satellite and in situ measurements in nearshore South Africa waters [41] further highlight these challenges.

Recent developments within the Global Ocean Observing System (GOOS) have increasingly focused on the use of autonomous uncrewed surface vehicles (USVs) to address these observational gaps [42]. The Sailbuoy, a wind-driven USV, has emerged as a robust platform for sustained environmental monitoring in challenging boundary current environments [42,43]. Unlike traditional drifters, USVs are steerable, enabling targeted sampling across sharp thermal fronts and sustained operation within highly dynamic coastal regions [35]. Previous studies have demonstrated their effectiveness for satellite validation in regions such as the California Current [34], the Arctic [44], the Southern Ocean [45] and trans-Pacific transects [46], highlighting their ability to provide high-frequency observations at temporal scales far exceeding satellite overpass frequency. Comparisons of air–sea flux measurements from an unmanned surface vehicle and established observing platforms have also demonstrated the potential of USVs for collecting oceanographic measurements [47]. However, comparable high-resolution, USV-based validation studies remain limited in the Agulhas Current region. The deployment of USVs within the Agulhas Current-shelf transition zone provides a unique opportunity to capture the rapid evolution of SST associated with fine-scale ocean processes that are often poorly resolved by global satellite products. These platforms offer a high-resolution observational framework for evaluating

satellite SST performance in one of the most dynamically complex coastal regions in the Southern Hemisphere.

This study evaluates the performance of multiple satellite SST products in the Agulhas Current-influenced coastal environment. Using high-resolution in situ observations collected by a Sailbuoy USV, we quantify the agreement between satellite-derived and in situ SST measurements. By accounting for differences in satellite observational approaches, we compare products across different processing levels and examine their capacity to resolve fine-scale variability associated with mesoscale and submesoscale processes. Through this approach, the study provides a comprehensive assessment of the performance of satellite SST products that are used for applications in energetic coastal and western boundary current systems.

2. Materials and Methods

2.1. Study Area

The study area lies along the southeast coast of South Africa, encompassing Algoa Bay and the surrounding region (Figure 1a). The region includes coastal and offshore waters influenced by the Agulhas Current along the continental shelf edge. The spatial extent of the analysis is defined by the trajectories of the Sailbuoy USV deployments conducted during the 2024 (purple) and 2025 (orange) surveys (Figure 1a). These tracks sample variability across both nearshore and offshore environments and form the basis for the satellite–in situ SST comparisons presented in this study. The observing platform used to acquire in situ measurements is shown in Figure 1b,c.

2.2. Sailbuoy Observations

The primary in situ SST dataset used for this validation study was collected using the Sailbuoy PimPim (SB2326), developed by Offshore Sensing AS (Sandsli, Norway) [48] and operated by the University of Gothenburg. The Sailbuoy is an autonomous uncrewed surface vehicle (USV) equipped with integrated oceanographic and meteorological sensors (Figure 1b), enabling sustained observations in remote under-sampled marine environments [42]. The platform is wind-propelled and solar-powered, allowing for long-endurance missions of up to 12 months, with real-time data transmission and control maintained via the Iridium satellite system (Figure 1b). For this study, SST data were derived from the RBR Legato Conductivity, Temperature and Depth (CTD) sensor (RBR Ltd., 2025; Ottawa, ON, Canada). The temperature sensor has a specified accuracy of ±0.002 °C over the range of −5 °C to +35 °C and a resolution of <0.00005 °C, making it well-suited for satellite validation applications. Temperature measurements were recorded at an approximate depth of 1 m, representing bulk SST [1]. Sailbuoy SST observations, provided at 10 min intervals, were checked for missing values and inspected for abrupt temporal changes. Potential anomalies were assessed in relation to the surrounding SST evolution, geographic position and concurrent salinity measurements. Rapid temperature changes were not automatically classified as errors, given the potential for genuine oceanographic variability. No observations were excluded following this assessment.

The Sailbuoy was also equipped with an Aanderaa DCPS 5400 Acoustic Doppler Current Profiler (ADCP; Aanderaa Data Instruments AS, Bergen, Norway) for current velocity measurements, an FT742 wind sensor (FT Technologies Ltd., Sunbury-on-Thames, UK) for wind speed and direction, and a Telaire T9602 sensor (Amphenol Advanced Sensors, St. Marys, PA, USA) for air temperature and relative humidity (Figure 1b), enabling concurrent characterisation of atmospheric and oceanographic conditions during the deployments [49]. The Sailbuoy was deployed during two surveys conducted as part of an African Coelacanth Ecosystem Programme (ACEP) project designed to understand the impacts of the Agulhas

Current on coastal and shelf ecosystems. It was launched from the RV Observer along a sampling line intersecting Algoa Bay perpendicularly (Figure 1a). The first deployment began on 8 May 2024 at 34.01°S, 26.11°E and sampled the coastal waters for 44 days before being retrieved on 20 June 2024 (Figure 1a). The second deployment began on 6 February 2025 at 33.78°S, 26.10°E. This mission lasted 28 days, after which the platform was recovered near Plettenberg Bay on 7 March 2025 (Figure 1a). However, the available dataset extended only to 5 March 2025. During both missions, SST was recorded as 1 min averages sampled at 10 min intervals along the Sailbuoy trajectory, providing a continuous, high-frequency, near-surface dataset for evaluating satellite-derived SST [1,20] in the dynamic regions inshore of the Agulhas Current within a range of 4.7 to 60.0 km from the coast.

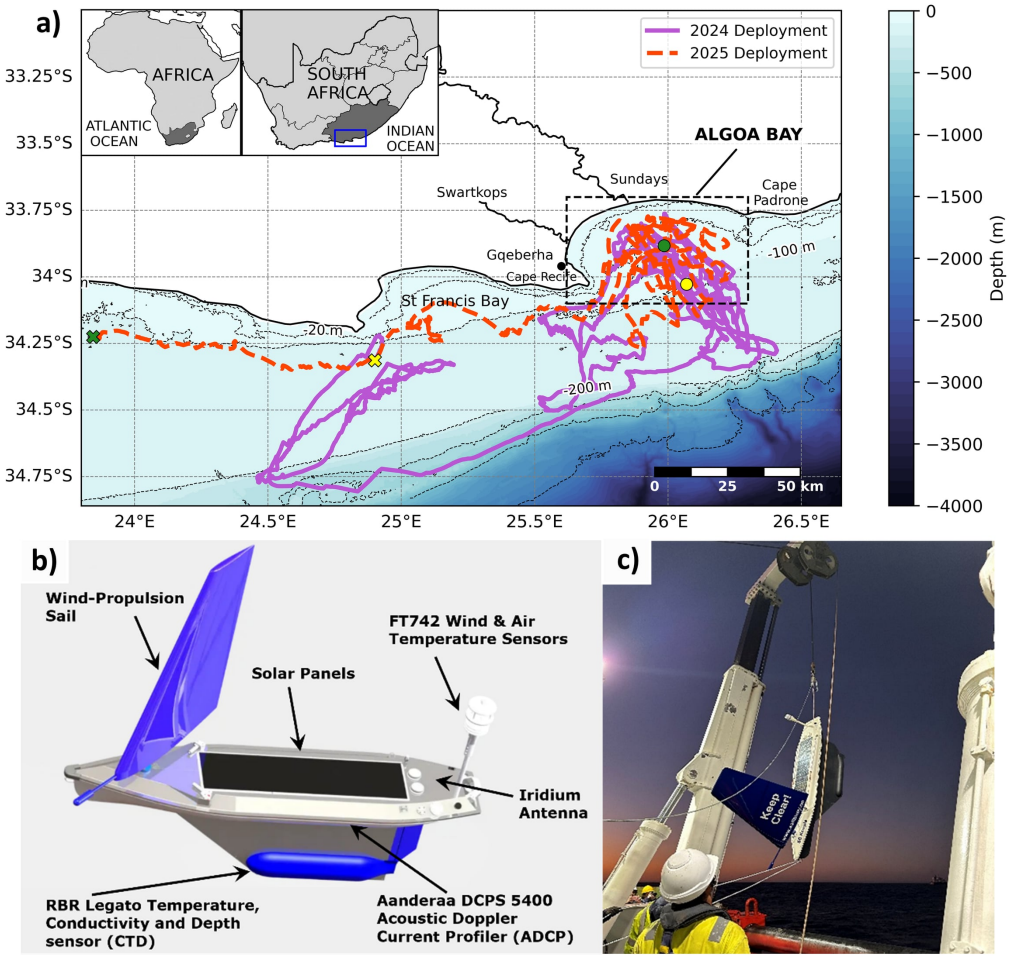

Figure 1. (**a**) Map of the study area along the southeast coast of South Africa showing the trajectories of the Sailbuoy during the May–June 2024 (solid purple) and February–March 2025 (dashed orange) surveys in Algoa Bay (dashed black box) and the surrounding region. Yellow (2024) and green (2025) markers indicate deployment (circles) and recovery (crosses) locations, respectively. Background shading represents bathymetric depth (m), with contours shown as black dashed lines; the 100 m and 200 m isobaths highlight the continental shelf break and upper slope. (**b**) Schematic of the Sailbuoy with onboard sensors indicated. (**c**) The Sailbuoy during deployment from the RV SA Agulhas II.

2.3. Satellite Data Products

This study used five distinct SST satellite products, consisting of one Level 2 (L2), two Level 3 (L3), and two Level 4 (L4) datasets. These represent instantaneous swath observations, gridded composites and daily gap-filled analyses, respectively, at varying spatial resolutions (Table 1).

Table 1. Summary of satellite Sea Surface Temperature datasets used in this study.

Product	Sensor	Level	Resolution (°)	SST Type
Sentinel-3	SLSTR	L2	0.01	Skin
MODIS Aqua	MODIS on board Aqua	L3	0.04	Skin
VIIRS	VIIRS on board Suomi-NPP	L3	0.04	Skin
OSTIA	AVHRR, VIIRS, SEVIRI, AMSR-2, IASI, TMI, SSMI/S	L4	0.05	Foundation
MUR	MODIS, AVHRR, AMSR-E, AMSR-2, WindSa	L4	0.01	Foundation

Note: SLSTR: Sea and Land Surface Temperature Radiometer; MODIS: Moderate Resolution Imaging Spectroradiometer; VIIRS: Visible Infrared Imaging Radiometer Suite; AVHRR: Advanced Very High Resolution Radiometer; SEVIRI: Spinning Enhanced Visible and Infrared Imager; AMSR-2/AMSR-E: Advanced Microwave Scanning Radiometer; IASI: Infrared Atmospheric Sounding Interferometer; TMI: TRMM Microwave Imager; SSMI/S: Special Sensor Microwave Imager Sounder.

2.3.1. Level 2 and Level 3 Infrared SST Products

The L2 dataset comprised the Sea and Land Surface Temperature Radiometer (SLSTR) observations onboard Sentinel-3B, provided by the European Organisation for the Exploitation of Meteorological Satellites [50]. These data are acquired at a native swath resolution of 0.01° (~1 km) with sub-daily temporal coverage. To enhance SST retrieval accuracy, the SLSTR instrument employs a dual-view configuration for improved atmospheric correction [19,51]. For consistency with other datasets and to facilitate subsequent analysis, individual swath files were aggregated into daily datasets. Quality control was applied using the associated flags to exclude pixels affected by cloud contamination or low-confidence retrievals [14].

The L3 datasets included SST products from the Moderate Resolution Imaging Spectroradiometer (MODIS) aboard NASA's Aqua satellite and the Visible Infrared Imaging Radiometer Suite (VIIRS) on the Suomi National Polar-orbiting Partnership (Suomi-NPP) satellite. These data were obtained from the NASA EarthData portal (https://search.earthdata.nasa.gov/, accessed on 22 September 2026) [52]. These two mapped products are provided as daily composites on a regular geographic grid with a spatial resolution of 0.04° (~4 km). Since they rely on infrared sensors, both L2 and L3 products are limited to clear-sky conditions, as cloud cover obstructs SST retrievals. Under these conditions, the sensors measure the skin temperature, representing the upper 10–20 μm of the ocean surface [1,53]. As with the L2 data, standard quality flags were applied to remove unreliable retrievals from MODIS and VIIRS observations.

2.3.2. Level 4 Multi-Sensor SST Products

The L4 datasets comprised two multi-sensor analysed products from the Group for High-Resolution Sea Surface Temperature (GHRSST) framework: the Operational Sea Surface Temperature and Ice Analysis (OSTIA) and the Multi-scale Ultra-high Resolution (MUR) v4.1 SST product. OSTIA is distributed by the Copernicus Marine Environment Monitoring Service (CMEMS; https://marine.copernicus.eu/, accessed on 22 September 2026) [54] and is a daily gap-free 0.05° (~5 km) resolution product developed by the UK Met Office using optimal interpolation [55,56]. It assimilates both daytime (for wind speeds > 6 m s^{-1}) and nighttime observations from multiple infrared and microwave sensors (Table 1), as well as in situ data from ships and drifting or moored buoys [8,17] The MUR dataset is distributed by NASA's Jet Propulsion (JPL) Physical Oceanography Distributed Active Archive Centre (PO.DAAC; https://podaac.jpl.nasa.gov/, accessed on 22 September 2026). The product provides a higher spatial resolution of 0.01° (~1 km) and is developed using a Multi-Resolution Variational Analysis (MRVA) technique for data assimilation and interpolation [18]. In contrast to OSTIA, MUR relies exclusively on

nighttime observations to minimise the influence of diurnal warming and integrates SST observations from multiple platforms (Table 1), as well as in situ observations from the NOAA's iQuam project [18].

Both L4 products combine satellite and in situ observations to produce spatially and temporally complete SST fields. By leveraging the high resolution of infrared sensors and the cloud-penetrating capabilities of microwave radiometers, these L4 analyses represent foundation SST, defined as the temperature at depths (~1–10 m) below the diurnal warm layer after the influence of daytime solar heating has largely dissipated. This results in a reduced influence of short-term surface heating and small-scale variability compared to L2 and L3 products [1,17,18,57]. The satellite-derived SST were compared against the in situ Sailbuoy observations for the periods 8 May to 20 June 2024 and 6 February to 5 March 2025 to evaluate the satellite performance in the dynamic Agulhas Current region. The satellite and Sailbuoy datasets were subsequently collocated in space and time for statistical evaluation.

2.4. Statistical Comparison Analysis

To evaluate satellite SST performance against the in situ Sailbuoy observations, a multi-tier statistical validation framework was implemented, accounting for the differing spatial and temporal characteristics of the L2, L3 and L4 datasets (Table 1). Following data acquisition and quality control [18], all satellite datasets were standardised to a daily temporal resolution to enable consistent comparison. The gridded L3 (MODIS and VIIRS) and L4 (OSTIA and MUR) datasets were used at their native daily resolution, while L2 Sentinel-3 swaths were aggregated into 24 h composites to improve spatial coverage and minimise cloud-related gaps in the Algoa Bay region [11,40]. While this harmonisation ensures consistent comparison with the Sailbuoy, differences in temporal representation remain, as Sentinel-3 retains greater sensitivity to sub-daily variability relative to the daily L3 and L4 products. These differences were considered in the interpretation of the results.

Matchup pairs were generated using a nearest-neighbour spatial approach, whereby the closest cloud-free, quality-controlled satellite pixel was extracted for each 10 min Sailbuoy observation. Matchup distances were summarised by processing level for each survey period. The average matchup distance for L2 (Sentinel-3) was 0.39 ± 0.15 km in 2024 and 0.38 ± 0.15 km in 2025. Average matchups across all three L3 products (MODIS and VIIRS) were 1.41 ± 0.59 km in 2024 and 1.90 ± 1.70 km in 2025, consistent with the coarser spatial resolution and increased sensitivity to cloud-contaminated sampling. L4 products exhibited effectively negligible collocation uncertainty relative to their native spatial resolution and spatial smoothing scales and were therefore not included in quantitative matchup distance reporting.

Due to the daily temporal resolution of the satellite fields, multiple high-frequency Sailbuoy observations within a given day were often associated with the same corresponding daily satellite value. To minimise the influence of sub-daily variability and sampling mismatches, both the Sailbuoy observations and collocated satellite values were subsequently averaged to daily means, producing matched daily satellite–Sailbuoy pairs. This approach preserves the spatial variability sampled along the Sailbuoy trajectory, while ensuring consistency with the temporal resolution of the satellite datasets. However, it may introduce mismatches between instantaneous satellite observations and temporally averaged Sailbuoy measurements. Additionally, implicit weighting of satellite values may occur where multiple Sailbuoy observations fall within the same satellite pixel. These effects are expected to be more pronounced for the L2 and L3 products as they rely on discrete overpasses and cloud-free retrievals [1]. As a result, daily representations derived from L2 and L3 data may not fully capture sub-daily variability, leading to greater representative-

ness differences when compared to temporally averaged Sailbuoy observations. Although temporal mismatches may also affect the L4 products, their blended and temporally interpolated nature provides more continuous daily coverage, potentially reducing sensitivity to data gaps.

The performance of each satellite product was evaluated using a suite of standard statistical metrics. The mean bias error (residuals) and root mean square error (RMSE) were used to quantify the systematic offset and the error magnitude of the deviations, respectively:

$$MBE = \frac{1}{N}\sum_{i=1}^{N}(S_i - SB_i)$$

$$RMSE = \sqrt{\frac{1}{N}\sum_{i=1}^{N}(S_i - SB_i)^2}$$

where S_i and SB_i denote the satellite-derived and Sailbuoy SST values, respectively, and N is the number of daily matched observations.

Matchup consistency was assessed using linear regression analysis, with the Pearson correlation coefficient (r), coefficient of determination (R2), regression slope and standard error used to quantify the strength and agreement of the relationship. Statistical significance was evaluated at the 99% confidence level ($p < 0.01$). To account for temporal autocorrelation between consecutive daily matchups, the statistical significance of Pearson correlation coefficients was reassessed using an effective sample size approach based on the method of [58].

3. Results

3.1. Overview of Sailbuoy SST Variability and Oceanographic Dynamics

The Sailbuoy observations reveal spatial and temporal variability in SST and near-surface circulation across both survey periods (Figure 2). Distinct differences are evident between the 8 May to 20 June 2024 (hereafter referred to as the 2024 survey) and 6 February to 5 March 2025 (hereafter referred to as the 2025 survey) deployments, reflecting seasonal contrasts and inherent variability in regional oceanographic conditions.

During the 2024 survey (Figure 2a), the Sailbuoy initially sampled warm waters within and along the outer shelf of Algoa Bay, with SSTs ranging between 18 °C and 21 °C. As the Sailbuoy transited southwest across the shelf towards the 500 m isobath, SSTs decreased to about 16 °C by 29 May. These cooler waters extended northeast as the Sailbuoy re-entered Algoa Bay, with temperatures further decreasing to around 15 °C, despite warmer temperatures (18–21 °C) having been recorded in the same area approximately 10 days earlier. On 10 June, the Sailbuoy sampled along the shelf break (between the 500 and 1000 m isobaths), where it encountered the highest temperatures of the survey (24 °C, Figure 2a), coinciding with a strong southwestward flow (>1.0 m s^{-1}) until 12 June. SSTs subsequently decreased (<21 °C) as the Sailbuoy returned towards the inner shelf on 13 June, further southwest along the coast. The spatial distribution of SST (Figure 2a) highlights strong horizontal gradients, particularly across the shelf break, where strong near-surface currents associated with the Agulhas Current contrasted with localised variability and directional changes closer to the coast. Together, these patterns reflect a dynamically structured environment during the 2024 survey, characterised by cross-shelf variability and periods during which the Sailbuoy sampled offshore waters of the Agulhas Current.

In contrast, the 2025 survey (Figure 2b) was characterised by overall warmer SSTs within Algoa Bay and enhanced along-track SST gradients (mean ± SD: 0.14 ± 0.22 °C km^{-1}) compared to 2024 (0.10 ± 0.19 °C km^{-1}). During the early phase of the mission, the Sailbuoy remained within Algoa Bay, where SSTs were relatively uniform and exceeded 20 °C, with no

clear indication of cold-water intrusions. After 26 February, the platform transitioned into a sustained westward trajectory parallel to the coastline (Figure 2b). Along this track, SSTs exhibited substantially greater variability, ranging from ~10 °C to ~22 °C. A pronounced cooling event was observed as the Sailbuoy moved westward, with temperatures decreasing from ~20 °C to below 12 °C within three days, reaching lows of ~10 °C in regions east of 25°E and west of 24.5°E. Between these regions, the Sailbuoy moved slightly offshore, away from the coastal upwelling and sampled warmer water. This cold-water coincided with strong offshore currents exceeding 0.5 m s^{-1}, consistent with an upwelling event along the inner shelf. The observed SST variability along the Sailbuoy track indicates a pronounced east–west gradient, with cooler waters (~10–18 °C) encountered in the western portion of the domain and warmer waters (20–22 °C) within Algoa Bay. However, given the Lagrangian nature of the sampling, this gradient may reflect temporal aliasing associated with the progressive sampling of an evolving upwelling system.

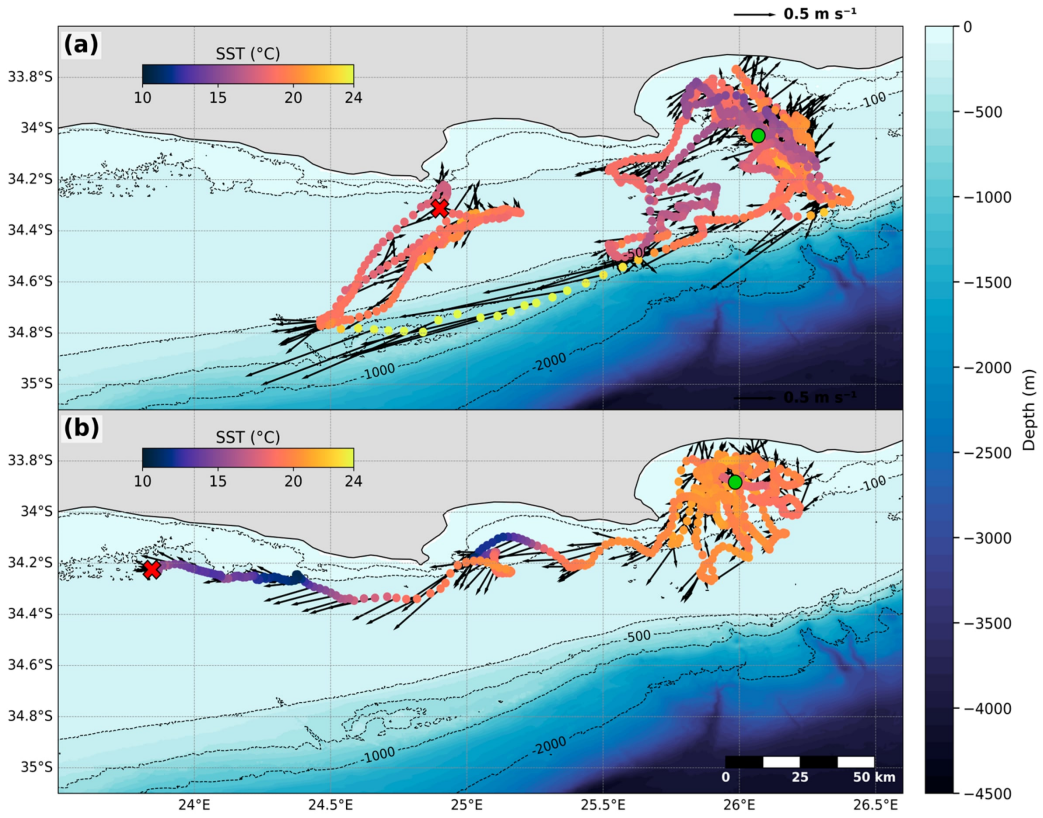

Figure 2. Spatial representation of Sailbuoy sampling and oceanographic conditions during the two surveys. Panels (**a**,**b**) show the bulk SST (°C) sampled along the Sailbuoy trajectories during the May–June 2024 and February–March 2025 surveys, respectively, with black vectors indicating 2-hourly near-surface currents. Green dots mark the deployment locations and red crosses mark the recovery locations for each survey. Background shading represents bathymetric depth (m), with black dashed contours indicating isobaths; the 100 m and 200 m isobaths highlight the continental shelf break and upper slope.

Compared to the 2024 survey, near-surface currents in 2025 were less variable, with lower mean speeds (0.26 ± 0.15 m s^{-1} compared to 0.30 ± 0.28 m s^{-1}) and reduced directional variability (circular standard deviation: 93° vs. 118°), indicating a more constrained flow regime, with a narrower spread of current directions and weaker velocity fluctuations. Short-lived deviations were still present during the cold-water intrusion period, despite the reduced current variability. The orientation of the strongest thermal gradients differed between the two surveys. In 2024, the sharpest SST gradients (0.148 ± 0.341 °C km^{-1})

were aligned with the outer continental shelf break and slope, reaching 3.78 °C km^{-1}, closely following the topographically steered pathway of the Agulhas Current along the 500 m to 1000 m isobaths. In contrast, during late February/early March of the 2025 survey, mean gradients increased (0.210 ± 0.242 °C km^{-1}), but the maximum value was lower (1.16 °C km^{-1}) and was concentrated on the inner continental shelf, landward of the 100 m isobath, coinciding with the boundary of the cold-water intrusion (Figure 2a,b). This reflects the fact that the Sailbuoy did not sample the Agulhas Current during the 2025 deployment and therefore did not encounter the strong shelf-edge thermal gradients observed in 2024. Overall, the observations demonstrate pronounced spatial gradients, temporal variability, and complex circulation patterns across the study region at meso- and submesoscale scales.

3.2. Spatiotemporal Comparison of Sailbuoy and Satellite SST

We compare the in situ Sailbuoy SST observations from the 2024 and 2025 missions with multiple co-located satellite-derived SST products, from L2 to L4, to evaluate their performance within the dynamic Agulhas Current coastal system.

3.2.1. Sentinel-3 (L2)

During the 2024 survey (Figure 3a,b), Sentinel-3 exhibited a strong agreement with the Sailbuoy ($r = 0.86$, $p < 0.01$), explaining approximately 74% of the observed variance in SST. Early in the deployment (10–21 May), Sentinel-3 recorded SSTs up to 1 °C cooler than the Sailbuoy and generally tracked the lower bound of the daily SST range, contributing to an overall cool bias of −0.20 °C. This systematic underestimation is further reflected in the scatter distribution (Figure 3b), where values at the lower thermal range (16–20 °C) lay below the 1:1 line. Conversely, SSTs exceeding 20 °C clustered above the 1:1 line, indicating warmer satellite estimates at higher temperatures. This was visually evident during the warming phase after 7 June, where Sentinel-3 reached a peak (~23 °C) higher than the Sailbuoy (~21 °C), albeit still within the Sailbuoy-observed daily range. Sentinel-3 SST closely tracked the Sailbuoy SST as the USV traversed both the shelf and offshore regions, with largest deviations mainly during periods of rapid change (e.g., 1 and 6 days of +4 °C and −5 °C, respectively), yielding an RMSE of 0.74 °C (Table 2). The regression slope of 1.10 indicated that Sentinel-3 reproduced the amplitude of observed SST variability well during the 2024 survey.

Despite persistent cloud cover reducing the number of valid matchups in 2025 (Figure 4a,b; Table 2), Sentinel-3 maintained a strong relationship with the Sailbuoy ($r = 0.84$, $p < 0.01$), explaining 71% of the observed variance. Furthermore, Sentinel-3 displayed a near-zero bias of +0.06 °C, indicating minimal systematic offset, while its RMSE decreased slightly to 0.68 °C. However, the sensitivity to localised features increased substantially, with the regression slope decreasing to 0.70. This can be linked to the satellite's response during the intense early March cooling event (Figure 4a). Between 28 February and 3 March, thermal gradients caused daily ranges to span up to 8 °C, with Sailbuoy minima approaching 11 °C. While Sentinel-3 underestimated the intensity of this cooling by ~3 °C, the satellite observations remained largely within the Sailbuoy's daily temperature range. These discrepancies are illustrated in the scatter distribution (Figure 4b), which shows tight clustering at warmer SSTs (18–21 °C) and increasing divergence at colder temperatures, highlighting the difficulty of resolving the full magnitude of coastal cooling events.

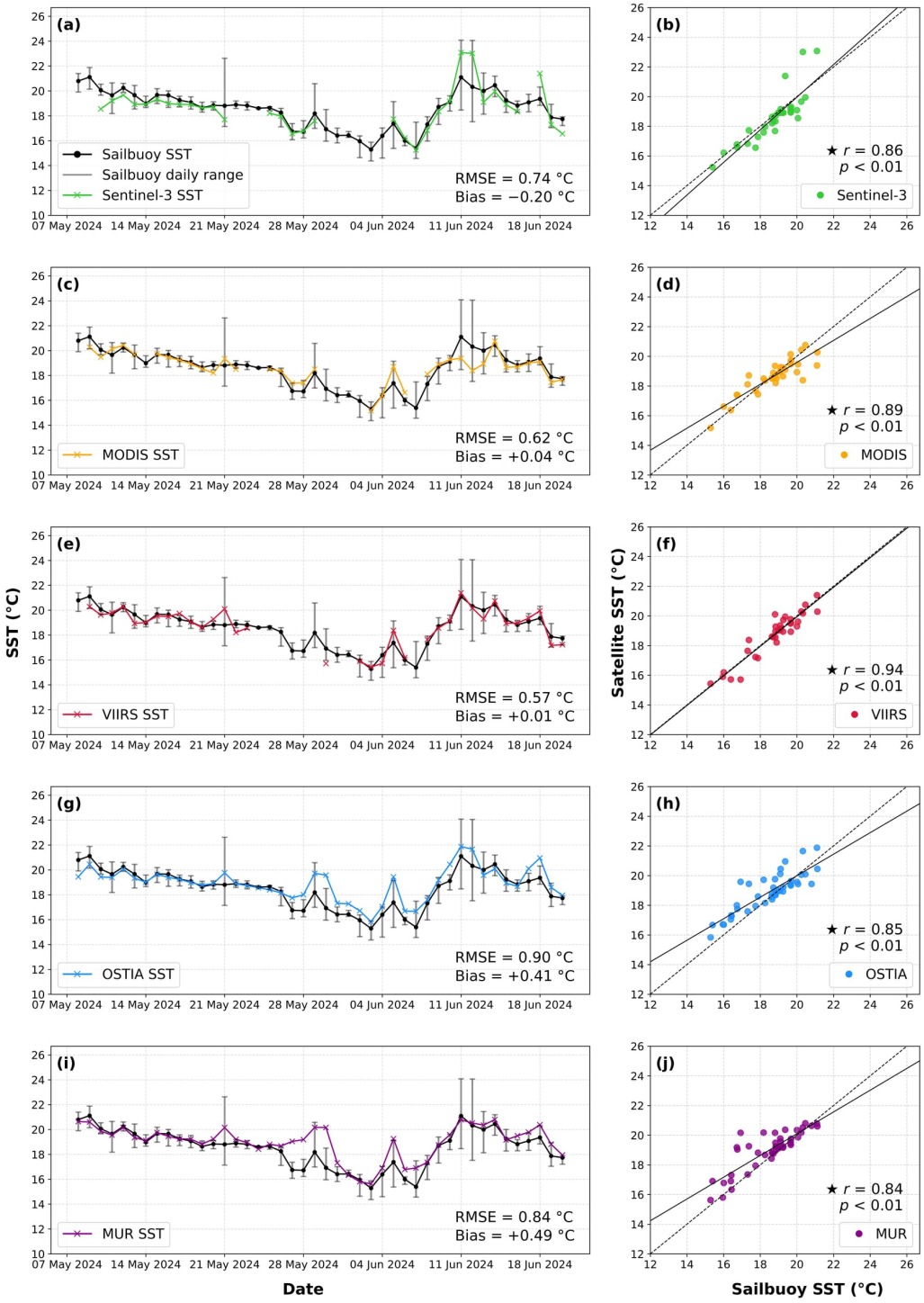

Figure 3. Time series comparisons (left panels) and corresponding scatter distributions (right panels) between daily averaged Sailbuoy SST observations and collocated satellite-derived SST products during the 2024 survey. Each row displays daily averaged Sailbuoy SSTs (black circles) alongside satellite SSTs for (**a**,**b**) Sentinel-3 (L2; green), (**c**,**d**) MODIS (L3; yellow), (**e**,**f**) VIIRS (L3; red), (**g**,**h**) OSTIA (L4; blue), and (**i**,**j**) MUR (L4; purple). Grey vertical bars in the left panels represent the full daily temperature range recorded by the Sailbuoy from 10 min observations. Gaps in the satellite time series correspond to periods with no valid SST retrievals due to cloud cover. In the right panels, the solid black line represents the linear regression fit, while the dashed black line indicates the 1:1 relationship. The root mean square error (RMSE; °C), bias (°C), Pearson correlation coefficients (r) and associated p-values are shown, with statistically significant correlations ($p < 0.01$) indicated by a star.

Table 2. Comparative validation statistics for five satellite SST products: Sentinel -3, Moderate Resolution Imaging Spectroradiometer (MODIS), (Visible Infrared Imaging Radiometer Suite) VIIRS, Operational Sea Surface Temperature and Ice Analysis (OSTIA), Multi-scale Ultra-high Resolution (MUR) against Sailbuoy observations. Shown for each survey (May–June 2024 = grey; February to March 2025 = white) are the number of matchups (n), correlation coefficients (r-value), regression slope (m), Standard Error (SE) of regression, root mean square error (RMSE; °C), bias (°C) and the percentage of satellite SST observations within the Sailbuoy daily temperature range (%). RMSE and bias are reported with 95% bootstrap confidence intervals.

Product	Year	n	r-Value	Slope (m)	SE (°C)	RMSE (°C), 95% CI	Bias (°C), 95% CI	Satellite SST Within Sailbuoy Daily Range (%)
Sentinel-3	2024	32	0.86	1.10	0.12	0.74 (0.55–0.96)	−0.20 (−0.41–0.03)	88
	2025	15	0.84	0.70	0.12	0.68 (0.46–1.00)	+0.06 (−0.17–0.30)	80
MODIS	2024	35	0.89	0.74	0.07	0.62 (0.49–0.76)	+0.04 (−0.14–0.23)	91
	2025	17	0.44	0.16	0.08	0.73 (0.44–1.09)	−0.23 (−0.62–0.23)	76
VIIRS	2024	34	0.94	0.99	0.06	0.57 (0.42–0.73)	+0.01 (−0.15–0.17)	88
	2025	20	0.46	0.32	0.14	0.76 (0.43–1.19)	+0.28 (−0.14–0.81)	75
OSTIA	2024	44	0.85	0.73	0.07	0.90 (0.72–1.09)	+0.41 (0.18–0.65)	70
	2025	28	0.91	0.55	0.05	1.10 (0.67–1.65)	+0.51 (0.04–1.08)	78
MUR	2024	44	0.84	0.73	0.07	0.84 (0.60–1.13)	+0.49 (0.22–0.81)	79
	2025	28	0.54	0.43	0.13	2.23 (1.38–3.19)	+1.91 (1.05–2.86)	43

Note: All correlations were statistically significant ($p < 0.01$), except for MODIS ($p = 0.07$), VIIRS ($p = 0.10$) and MUR ($p = 0.03$) during 2025. Bias values are reported to two decimal places; the unrounded VIIRS bias was +0.006 °C.

3.2.2. MODIS (L3)

In 2024, MODIS (L3) showed strong statistically significant agreement with Sailbuoy observations ($r = 0.89$, $p < 0.01$), explaining approximately 79% of the observed SST variability (Table 2). MODIS effectively reproduced the broad thermal evolution of the survey (Figure 3c,d). Most observations (91%) remained within the Sailbuoy's daily SST range, resulting in a low RMSE of 0.62 °C and near-zero overall bias of +0.04 °C. This minimal systematic bias is evident in scatter points clustering tightly near the 1:1 line (Figure 3d) despite localised periods of over- and underestimations (up to 2 °C). This behaviour was particularly evident from 10 to 13 June, where MODIS underestimated the Sailbuoy daily mean temperature (~2 °C), though values remained within the lower bounds of the Sailbuoy's daily range. This is further supported by the regression slope of 0.74, suggesting reduced representation of the observed SST range during short-term variability.

In contrast, the 2025 survey highlighted distinct limitations of the MODIS sensor during highly dynamic cold-water intrusions (Figure 4c,d). Persistent cloud cover during the cooling event produced extensive data gaps, causing matchups to decrease by almost half relative to 2024 (Table 2). Consequently, the correlation weakened substantially (r = 0.44) and lost statistical significance at the 0.01 level (Figure 4d). While the RMSE increased by 0.1 °C and the standard error remained relatively unchanged, the regression slope decreased sharply to 0.16. Furthermore, MODIS exhibited a shift from a weak warm bias to an overall cool bias of −0.23 °C. The observations were concentrated within a warmer SST range (18–20 °C) and failed to capture the intense cooling (~14–17 °C) recorded in situ (Figure 4d). Although similar cloud-driven data gaps impacted Sentinel-3 (Figure 4a), MODIS exhibited poorer overall agreement with the Sailbuoy observations. However, these statistics were strongly influenced by two MODIS data points during the most intense phase of the cooling event, while the remaining observations showed considerably closer agreement with the Sailbuoy.

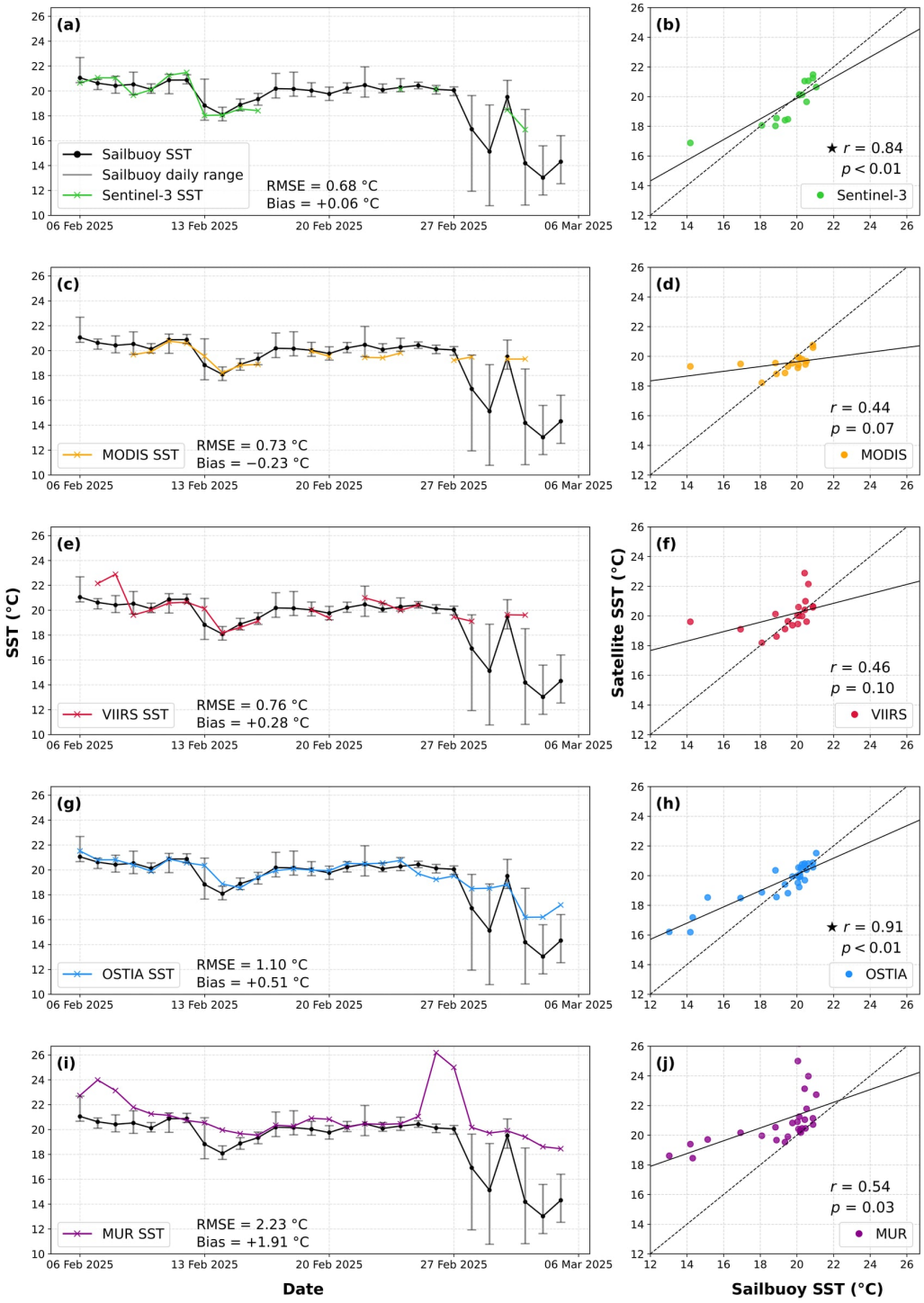

Figure 4. Time series comparisons (left panels) and corresponding scatter distributions (right panels) between daily averaged Sailbuoy SST observations and collocated satellite-derived SST products during the 2025 survey. Each row displays daily averaged Sailbuoy SSTs (black circles) alongside satellite SSTs for (**a**,**b**) Sentinel-3 (L2; green), (**c**,**d**) MODIS (L3; yellow), (**e**,**f**) VIIRS (L3; red), (**g**,**h**) OSTIA (L4; blue), and (**i**,**j**) MUR (L4; purple). Grey vertical bars in the left panels represent the full daily temperature range (minimum–maximum) recorded by the Sailbuoy from 10 min observations. Gaps in the satellite time series correspond to periods with no valid SST retrievals due to cloud cover. In the right panels, the solid black line represents the linear regression fit, while the dashed black line indicates the 1:1 relationship. The root mean square error (RMSE; °C), bias (°C), Pearson correlation coefficients (r) and associated p-values are shown, with statistically significant correlations ($p < 0.01$) indicated by a star.

3.2.3. VIIRS (L3)

VIIRS (L3) performed strongly in 2024 (Figure 3e,f), maintaining the highest statistically significant relationship with the Sailbuoy observations ($r = 0.94$, $p < 0.01$), and explaining approximately 88% of in situ thermal variance. This high precision was reflected by the lowest RMSE of 0.57 °C, an almost negligible overall bias of +0.006 °C, and a regression slope near unity ($m = 0.99$; Table 2). This indicated an excellent representation of both magnitude and timing of coastal SST variability. The time series confirms that VIIRS effectively resolved both stable thermal conditions early in the survey and the high-frequency fluctuations during June (0.86 ± 0.76 °C day^{-1}, Figure 3e). Most satellite observations (88%) remained strictly within the Sailbuoy's daily SST range, validating the sensor's capacity to resolve short-term thermal variability.

Similarly to the other infrared products, the agreement between VIIRS and Sailbuoy SST was weaker during the 2025 deployment (Figure 4e,f) than during 2024. Although its relationship with the Sailbuoy remained marginally stronger than that of MODIS ($r = 0.46$), the correlation was no longer statistically significant ($p > 0.01$; Figure 4f). The regression slope decreased to 0.32, while the standard error increased by 0.08 °C and the RMSE rose by 0.19 °C, indicating a reduced ability to reproduce Sailbuoy SSTs. The scatter plot (Figure 4f) reveals that while data points at the centre of the distribution are clustered near the 1:1 line, a pronounced divergence of up to 5 °C developed at both SST extremes. This manifested as an elevated overall bias of +0.28 °C driven by both early-survey overestimation, where satellite observations exceeded the Sailbuoy's daily range, and by the cooling event. As with the other infrared products, VIIRS overestimated (~5 °C) the rapid cooling between 28 February and 3 March.

3.2.4. OSTIA (L4)

During the 2024 survey, the gap-free blended OSTIA (L4) product reproduced the broad SST structure well (Figure 3g,h), maintaining a strong, statistically significant relationship with the Sailbuoy ($r = 0.85$; $p < 0.01$) and explaining 72% of in situ variability. While OSTIA successfully captured the timing of major thermal transitions (Figure 3g), it routinely overestimated their magnitude (by 1 °C on average). During late May through June, OSTIA SSTs were up to 2 °C warmer than the Sailbuoy daily means and occasionally exceeded the observed daily maximum temperature envelope. This consistent overestimation is reflected in an overall warm bias of +0.41 °C. The scatter distribution (Figure 3h) supports this trend, clustering above the 1:1 line. This contributed to a high RMSE of 0.90 °C, along with a regression slope of 0.73, indicating a moderate compression of the true dynamic coastal range.

During the 2025 survey, OSTIA continued to track the overall progression of SST variability and emerged as the highest-performing product for this deployment (Figure 4g,h). The correlation strengthened further ($r = 0.91$, $p < 0.01$), with its proportion of explained variance increasing to 83%. However, as a blended product, OSTIA heavily smoothed the sharpest thermal gradients, underestimating the true dynamic range during periods of extreme variability (Figure 4g,h). OSTIA failed to reproduce the full intensity of the late February/early March cooling event, remaining consistently warmer than the Sailbuoy's daily means by an increased averaged warm bias of +0.51 °C (Table 2) and occasionally exceeding the daily Sailbuoy maximum (Figure 4g). This smoothing led to substantial localised disagreement of up to 4 °C, where the colder Sailbuoy observations (~13–15 °C) corresponded to OSTIA temperatures of ~16 °C to 19 °C (Figure 4h). Consequently, the overall RMSE increased to 1.10 °C, while the regression slope decreased to 0.55, demonstrating that while continuous L4 coverage is not affected by cloud gaps, it severely compressed the captured magnitude of cooling events.

3.2.5. MUR (L4)

The MUR (L4) product exhibited behaviour broadly similar to OSTIA during the 2024 deployment (Figure 3i,j), successfully capturing the broad SST evolution with a strong, statistically significant relationship with the Sailbuoy ($r = 0.84$, $p < 0.01$) and explaining approximately 71% of observed thermal variability. The time series demonstrated that MUR effectively followed Sailbuoy trends but frequently overestimated SSTs during both cooling (27 May, 30 May and 7 June) and warming (29 May and 5 June) phases (by ~1 °C on average), occasionally exceeding the Sailbuoy's daily maximum (Figure 3i). Performance improved noticeably during the offshore warming period (7–15 June), when the satellite observations aligned closely with Sailbuoy daily means. The overestimation resulted in an overall warm bias of +0.49 °C, an RMSE of 0.84 °C and a regression slope of 0.73. The scatter plot (Figure 3j) highlights this persistent offset, with data points falling predominantly on or above the 1:1 line.

MUR experienced the most extreme shift as performance deteriorated during the 2025 survey (Figure 4i,j). Although it maintained a moderate positive correlation with the Sailbuoy observations ($r = 0.54$), this relationship was no longer statistically significant ($p = 0.03$). The relationship was marginally stronger than the cloud-compromised L3 products (Table 2), while the proportion of explained variance dropped to approximately 29%. The product exhibited severe smoothing and range compression, marked by a decrease in the regression slope to 0.43 and an increase in standard error by 0.06 °C. This degradation was reflected by a pronounced, warm bias of +1.91 °C and RMSE of 2.23 °C, the highest overall error among all the tested sensors. Scatter points revealed large positive deviations from the 1:1 line at both thermal extremes (Figure 4j), where Sailbuoy SSTs of 13 °C to 17 °C corresponded to MUR values of ~18 °C to 21 °C. Temporally, MUR frequently exceeded the Sailbuoy's daily temperature envelope during both stable and dynamic conditions (Figure 4i). Early in the survey and between 27 and 28 February, MUR's overestimation reached up to 6 °C despite a narrow (~1 °C) daily range. Ultimately, during the major cold-water intrusions, MUR failed to capture the cooling, retaining anomalously warm SSTs and producing localised offsets of up to 5 °C during this event.

All satellite products exhibited varying biases relative to the Sailbuoy observations, ranging from a cool bias for Sentinel-3 (−0.20 °C) to near-zero biases for MODIS (+0.04 °C) and VIIRS (+0.006 °C) in 2024 and larger warm biases for OSTIA and MUR (+0.41 °C to +1.91 °C) across the two surveys (Table 2). These comparisons involve different SST definitions, as described in Sections 2.2 and 2.3, which may contribute to the observed biases. In addition, the diurnal SST signal was assessed by averaging Sailbuoy observations for each hour of the day across each survey. The difference between maximum and minimum means was 0.34 °C (2024) and 0.44 °C (2025), suggesting that diurnal variability may contribute to differences between satellite and in situ observations at daily timescales. Furthermore, the 2025 validation results are based on 15 to 28 daily matchups per satellite product (Table 2). This relatively small sample size means that individual observations may have a substantial influence on the calculated validation statistics, particularly the RMSE and bias. The 95% bootstrap confidence intervals reported in Table 2 provide an indication of the uncertainty associated with these estimates. Therefore, differences in the reported errors between products should be interpreted with caution, as the limited sample size constrains the strength of conclusions about their relative performance.

3.3. Sensitivity Analysis: Impact of Cooling Events

To assess the influence of the cooling events on satellite performance during the 2025 survey, validation statistics were recalculated after excluding observations from the cooling event between 26 February and 5 March 2025 (Table 3), when all satellite products

exhibited their largest deviations from Sailbuoy measurements (Figure 4). Following this exclusion, the sensitivity analysis was based on 12–20 daily matchups per satellite product (Table 3). This reduced sample size should be considered when interpreting the results, as the calculated RMSE and bias may be more sensitive to the individual observations. The excluded period was characterised by a pronounced coastal cold-water intrusion associated with strong westward currents and substantial surface cooling across the study region (Figure 2b). On 28 February, upwelling-favourable easterly winds coincided with the development of strong SST gradients and the coastal expansion of a cold-water plume (Figure 5). These conditions were briefly interrupted by a relaxation on 1 March, and a reversal to south-westerly winds, before upwelling-favourable conditions resumed. The correspondence between wind forcing and the evolution of the cold-water plume provides evidence that the cooling event was associated with wind-induced upwelling (Figure 5c), providing the basis for the sensitivity analysis presented here.

Table 3. Sensitivity analysis of satellite sea surface temperature (SST) product performance following exclusion of the upwelling period (26 February–5 March 2025). Validation statistics are shown for five satellite SST products: Sentinel-3, Moderate Resolution Imaging Spectroradiometer (MODIS), Visible Infrared Imaging Radiometer Suite (VIIRS), Operational Sea Surface Temperature and Ice Analysis (OSTIA), and Multi-scale Ultra-high Resolution (MUR), against Sailbuoy observations. Metrics include the number of matchups (n), correlation coefficient (r-value), regression slope (m), standard error (SE) of regression, root mean square error (RMSE; °C), and bias (°C).

Product	n	r-Value	Slope (m)	SE (°C)	RMSE (°C)	Bias (°C)
Sentinel-3	12	0.92	1.23	0.17	0.52	+0.05
MODIS	13	0.85	0.69	0.13	0.56	−0.44
VIIRS	16	0.69	1.02	0.29	0.64	+0.17
OSTIA	20	0.78	0.73	0.14	0.60	+0.13
MUR	20	0.56	0.85	0.30	1.23	+0.91

Note: All correlations were statistically significant ($p < 0.01$), except for MUR ($p = 0.09$).

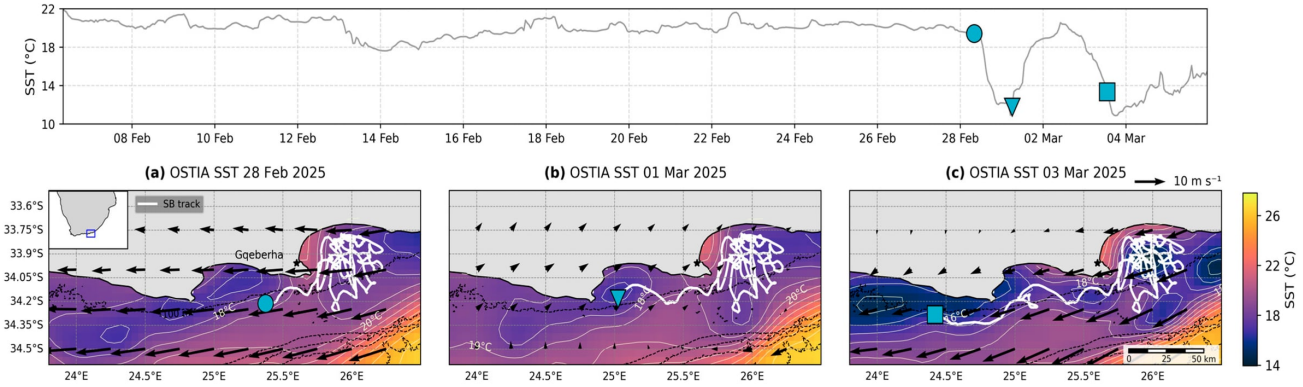

Figure 5. Spatial progression of the late February-early March wind-driven upwelling event along the east coast of South Africa during the 2025 Sailbuoy survey. The background fields (**bottom panels**) show L4 OSTIA SST (°C), with 1 °C isotherms (white) overlaid, and daily ERA5 10 m wind vectors (black arrows; 10 m s^{-1} reference in panel (**c**). The bold white track line shows the Sailbuoy trajectory up to the selected observation time in each panel, while the blue symbols indicate the corresponding Sailbuoy locations and link to the matching observations in the hourly in situ SST time series (**top panel**). Panels illustrate: (**a**) the onset of enhanced coastal wind forcing and associated surface cooling (28 February); (**b**) the first upwelling peak followed by a wind reversal and temporary surface warming (1 March); and (**c**) the second upwelling peak following the resumption of strong upwelling favourable winds (3 March).

The subsetted analysis therefore provides a clearer assessment of satellite performance under more moderate coastal conditions, enabling the sensitivity of each product to relatively extreme SST variability to be assessed. Extreme daily SST changes were identified as those exceeding the 90th percentile of the absolute day-to-day SST changes across the full-time series (2.479 °C day^{-1}). Three daily changes within the excluded period (28 February and 2–3 March 2025) exceeded this threshold. The exclusion window encompassed the broader evolution of the cooling event, identified from the Sailbuoy SST time series and the corresponding satellite–Sailbuoy differences, rather than only the individual days exceeding the threshold. The resulting metrics for this pre-cooling period indicate improved agreement with Sailbuoy observations across most products, although the magnitude of change varied between the satellites. Sentinel-3 exhibited the most stable behaviour under the filtered conditions, with correlation increasing to $r = 0.92$ ($p < 0.01$) and RMSE decreasing from 0.68 °C to 0.52 °C (Tables 2 and 3). The regression slope increased to 1.23, suggesting a slight overestimation of SST variability once the cooling event was removed. The standard error increased marginally, while bias remained negligible (+0.05 °C). These results indicate that Sentinel-3's performance is largely robust, with only limited sensitivity to the exclusion of upwelling conditions.

The most notable shift occurred within the L3 products (MODIS and VIIRS), both of which regained statistical significance ($p < 0.01$) during the filtered period. For MODIS, the correlation coefficient increased substantially from 0.44 to 0.85, while the regression slope rose from 0.16 to 0.69. RMSE decreased from 0.73 °C to 0.56 °C, although a persistent negative bias (−0.44 °C) emerged, indicating underestimation under more moderate variability conditions. VIIRS also improved, with correlation increasing to $r = 0.69$ ($p < 0.01$) and a reduction in RMSE relative to the full 2025 dataset. The regression slope (m = 1.02) suggests that VIIRS recovered its ability to represent the amplitude of SST variability once the cooling conditions were excluded, while bias remained weakly positive (+0.17 °C). Despite this improvement, VIIRS performance remained below that observed during the 2024 survey. The blended L4 products displayed contrasting responses, although both demonstrated reduced systematic error when filtered (Tables 2 and 3). OSTIA exhibited a decline in correlation from 0.91 to 0.78, but a substantial reduction in RMSE from 1.10 °C to 0.60 °C and in bias from +0.5 °C to +0.13 °C, indicating reduced overestimation of SSTs. The regression slope increased to 0.73, comparable to values observed during 2024, while the standard error increased from 0.05 °C to 0.14 °C. In contrast, MUR remained the least consistent product despite filtering with correlation remaining weak ($r = 0.56$). Although RMSE decreased relative to the full 2025 dataset, it remained high (1.23 °C), in addition to the bias (+0.91 °C), compared to all other products. The regression slope ($m = 0.85$) indicates partial improvement in variability representation, but persistent errors remain evident.

3.4. Impact of Sampling Availability on L4 SST Product Performance

While L4 products provide temporally complete datasets, their performance during the dynamically variable 2025 survey was notably reduced relative to the lower SST variability conditions observed during 2024 (Figure 4 and Table 2). To assess how L4 product performance changed under L3-constrained sampling conditions, OSTIA and MUR were re-evaluated using only days with valid MODIS and VIIRS retrievals (Table 4). This like-for-like comparison enables a direct assessment of L4 performance when restricted to the same days on which L3 retrievals were available and provides insight into how blending and interpolation influence SST representation relative to the complete L4 datasets. However, because cloud cover affects the availability of infrared SST retrievals, differences between the full and subset results may reflect both sampling differences and the environmental

conditions associated with the selected days. MODIS- and VIIRS-sampled days were used to define the L3-constrained subsets as these sensors constitute key infrared inputs commonly assimilated into L4 SST analyses, alongside other satellite and in situ observations [1,18]. Consequently, differences between the full-dataset and subset results may reflect both sampling availability and the environmental conditions associated with the selected days; this comparison does not isolate temporal sampling effects from environmental influences.

Table 4. Validation statistics for OSTIA and MUR SST products recalculated using only days with valid MODIS and VIIRS SST retrievals during the 2024 (grey) and 2025 (white) surveys. "All Days" refers to full daily matchups with Sailbuoy observations, while "MODIS-sampled" and "VIIRS-sampled" refer to subsets of OSTIA and MUR data matched only to days with valid MODIS and VIIRS SST retrievals, respectively. Metrics include the number of matchups (n), correlation coefficient (r-value), regression slope (m), standard error (SE) of regression, root mean square error (RMSE; °C), and bias (°C).

Product	Year	Sampling	n	r-Value	Slope (m)	SE (°C)	RMSE (°C)	Bias (°C)
OSTIA	2024	All Days	44	0.85	0.73	0.07	0.90	+0.41
		MODIS-sampled	35	0.86	0.79	0.08	0.87	+0.37
		VIIRS-sampled	34	0.85	0.77	0.09	0.88	+0.38
	2025	All Days	28	0.91	0.55	0.05	1.10	+0.51
		MODIS-sampled	17	0.91	0.64	0.07	0.85	+0.28
		VIIRS-sampled	20	0.90	0.65	0.07	0.83	+0.23
MUR	2024	All Days	44	0.84	0.73	0.07	0.84	+0.49
		MODIS-sampled	35	0.85	0.71	0.08	0.84	+0.47
		VIIRS-sampled	34	0.87	0.79	0.08	0.76	+0.37
	2025	All Days	28	0.54	0.43	0.13	2.23	+1.91
		MODIS-sampled	17	0.42	0.32	0.18	1.64	+1.37
		VIIRS-sampled	20	0.46	0.42	0.19	1.81	+1.50

Note: All correlations were statistically significant ($p < 0.01$), except for MUR during 2025 under MODIS-sampled (0.12) and VIIRS-sampled (0.11) conditions.

During the 2024 survey, both OSTIA and MUR exhibited only marginal sensitivity to temporal subsetting relative to their full-dataset performance (Tables 2 and 4). Correlations and regression slopes remained broadly consistent across the full dataset and both L3-sampled subsets, indicating minimal influence of temporal sampling. For OSTIA, the correlation (r = 0.85 to 0.86) and RMSE (0.90 °C to 0.87 °C) showed minor changes, while MUR maintained stable regression slopes (m = 0.71 to 0.79) and warm biases (+0.37 to +0.49 °C), regardless of the sampling mask applied. Minor improvements in Sailbuoy range representation were observed under clear-sky sampling conditions, with MUR showing the largest improvement under VIIRS-sampled conditions, where both RMSE and bias decreased by ~0.1 °C. These results indicate that the L4 product metrics were relatively insensitive to the temporal subsetting applied during the comparatively stable conditions of the 2024 survey.

In contrast, a pronounced sampling dependence emerged during the 2025 survey. Relative to the full-dataset results (Table 2), both OSTIA and MUR showed reduced RMSE and bias under L3-sampled conditions. OSTIA showed notable improvements in accuracy, with RMSE decreasing from 1.10° C in the full dataset to 0.85 °C (MODIS-sampled) and 0.83 °C (VIIRS-sampled), while the warm bias decreased by more than 50%, to +0.28 °C and +0.23 °C, respectively. Correlations and regression behaviour, however, remained broadly consistent with the full dataset. MUR also showed partial improvement under both MODIS- and VIIRS-sampled conditions but retained a pronounced warm bias (+1.37 to +1.50 °C), high RMSE (>1.60 °C), and weak correlations (r = 0.42 to 0.46) with low regression slopes (m = 0.32 to 0.42); neither correlation was statistically significant ($p > 0.01$). Thus, although

sampling availability reduced some of the error, MUR remained the least robust product across the sampling configurations.

When compared with the full L3 validation metrics (MODIS and VIIRS; Table 2), the subsampled L4 products showed some improvement but did not reach the performance of the L3 sensors observed during the 2024 survey. This discrepancy was more pronounced under the highly variable 2025 conditions, where MODIS and VIIRS, despite also exhibiting degraded performance, retained a closer representation of SST variability than MUR. These results suggest that MUR's poor performance during 2025 cannot be explained solely by differences in sampling availability. Its persistent warm bias, weak correlations and low regression slopes are also consistent with limitations in representing the large daily SST changes observed during the survey.

4. Discussion

The two Sailbuoy deployments sampled distinct oceanographic conditions along the southeast coast of South Africa, providing an opportunity for evaluating satellite SST performance under different environmental conditions. In May–June 2024, the Sailbuoy sampled a dynamically structured shelf environment, with pronounced cross-shelf SST variability and strong horizontal gradients associated with intermittent influence of the topographically steered Agulhas Current along the shelf break [11,59–61]. In contrast, rapidly evolving wind-driven coastal upwelling in February–March 2025, cooled SSTs by up to 6 °C over three days, consistent with previous descriptions of upwelling dynamics in the region [39,62,63]. These contrasting regimes therefore impose different observational challenges: the cross-shelf gradients during 2024 require sufficient spatial resolution to resolve frontal structure, whereas the rapid evolution of the 2025 upwelling event, combined with cloud-related data gaps, increases sensitivity to temporal sampling and the ability of satellite products to capture short-lived thermal extremes [64,65]. Accurately resolving these spatial and temporal changes in SST is important for characterising the fine-scale ocean processes that shape coastal physical and biological variability.

Satellite SST Performance Under Contrasting Coastal Conditions

Satellite SST performance differed between the two deployments, reflecting the contrasting oceanographic conditions sampled. The reduced accuracy observed during 2025 coincided with a rapidly evolving coastal upwelling event, strong SST variability, and reduced infrared sampling under persistent cloud cover. Differences in season, year and sampling track may also have contributed to the observed differences, and their individual effects cannot be separated within the present study. Together, these findings underscore the high sensitivity of satellite SST observations to rapid spatial and temporal variability in dynamic coastal waters.

The strong performance observed during 2024 indicates that both infrared (Sentinel-3, MODIS and VIIRS) and blended (OSTIA and MUR) satellite products were able to resolve the broader warm and cold water mass structure associated with shelf-break variability and intermittent Agulhas Current influence, despite the presence of sharp cross-shelf SST gradients, particularly near the shelf break. This is supported by the significant agreement with the Sailbuoy ($r = 0.84$ to 0.94), low RMSE values (<1 °C), and minimal systematic bias. Satellite observations also frequently fell within the daily SST range recorded by the Sailbuoy, suggesting that some apparent discrepancies relative to daily mean temperatures may reflect naturally occurring sub-daily variability rather than substantial disagreement between the datasets. This behaviour aligns with studies in other western boundary current systems and along the South African coastline, where satellite SST products generally

perform well under conditions dominated by large-scale frontal variability despite the presence of strong horizontal SST gradients [3,41,66].

In contrast, reduced satellite performance during the 2025 survey upwelling event appears to have been strongly influenced by the rapid evolution of the cooling and incomplete infrared sampling during the most dynamically active phase. Persistent cloud cover resulted in substantial data gaps in the infrared observations, meaning that the available satellite matchups did not capture the full range of cold SST conditions recorded by the Sailbuoy. Such sampling challenges have also been reported in previous studies [66,67], while the susceptibility of infrared retrievals to cloud-related data loss is well established [1]. The underestimation of SST by the satellite products is consistent with coastal validation studies, including those around South Africa where differences of up to 6 °C have been reported [41]. The sensitivity analysis showed that much of the reduced performance in 2025 was associated with the upwelling event rather than consistently poor agreement throughout the full-survey period. However, this comparison does not establish that the upwelling event alone caused the reduced performance, as the effects of oceanographic conditions, sampling availability and other differences between the surveys cannot be isolated. The most notable improvements were observed for MODIS and VIIRS after the late-February/early-March upwelling event was excluded, with both products regaining statistical significance with the Sailbuoy observations and showing improved representation of SST variability. This illustrates the challenges that extreme SST variability and extensive cloud cover associated with upwelling events pose for satellite-in situ comparisons.

Among the infrared products, Sentinel-3 exhibited the most stable performance across both surveys, with consistently high correlations (>0.84) and low RMSE, indicating greater stability under changing ocean conditions. Although it underestimated the peak cooling of the 2025 upwelling event, it captured variability better than MODIS and VIIRS. This performance reflects the advantages of SLSTR's dual-view atmospheric correction, which reduces satellite retrieval uncertainty [17,68], and L2 processing, which retains short-term and fine-scale variability that is often attenuated in L3 and L4 products [17]. Consequently, SLSTR is widely used for satellite SST calibration and bias correction [69]. In contrast, MODIS and VIIRS showed weaker agreement during 2025, with reduced correlations and increased scatter. Although cloud cover reduced matchup density across all infrared products, this effect had a stronger impact during the upwelling event and reflects a known limitation in cloud-prone coastal systems, including the South African coast [1,41]. However, this alone does not fully explain inter-sensor differences. Instead, performance reflects both differences in product processing and how the evolving SST field was sampled. Sentinel-3 benefits from a higher native spatial resolution (~1 km) than MODIS and VIIRS (~4 km), enabling improved representation of finer-scale thermal structures. Differences in overpass time may also contribute, with Sentinel-3 sampling during the mid-morning, while MODIS and VIIRS sample later in the day, when the surface thermal structure may have changed since the Sentinel-3 overpass and diurnal warming may be more pronounced [3]. Beyond this, L3 compositing reduces sensitivity to short-term variability, further limiting the ability to capture the full thermal range observed by the Sailbuoy [55]. Together, these factors provide plausible explanations for the differing ability of the L3 products to represent observed SST patterns during the 2025 upwelling event, while the sensitivity analysis demonstrates the strong influence of the event itself on overall validation performance.

To overcome cloud-induced observational gaps, L4 products use OI and multi-source blending to produce gap-free SST fields [18,26,55]. While this ensures spatial continuity, it introduces a trade-off between completeness and the ability to resolve the full magnitude of SST variability. OSTIA provided the most consistent L4 performance, maintaining strong agreement across both surveys. Both L4 products smoothed localised upwelling

signals, with MUR exhibiting the strongest attenuation of variability. This is consistent with previous studies around South Africa reporting reduced nearshore accuracy within ~30 km of the coast [70] and warm biases exceeding 2 °C in blended SST products [40,66]. Differences between the products likely reflect variations in their interpolation structure and input data constraints. In more extensively sampled regions such as the California Coastal System, both OSTIA and MUR have shown high correlations approaching 0.98, low biases and RMSE values with USV observations [34]. In contrast, reduced skill in resolving rapidly evolving coastal processes has been reported in energetic boundary current systems, including the Gulf Stream and Kuroshio Extension [30,71,72]. as well as in southern African coastal regions [66].

In this study, restricting the 2025 analysis to days with valid L3 retrievals reduced bias and RMSE for both L4 products, although the selected days may also have differed in their environmental conditions from the full survey. Clear-sky conditions can favour stronger solar warming and diurnal SST variability, which may increase vertical temperature gradients and contribute to differences between satellite-derived and Sailbuoy SST [73]. However, both L4 products showed improved agreement with the Sailbuoy under L3-constrained sampling conditions, despite the potential for diurnal variability to contribute to these differences. This suggests that the discrepancies observed during the full survey may not be explained solely by differences in the representation of near-surface temperature variability. The interpolation and blending used to generate spatially complete L4 fields may also limit their ability to represent SST variability during upwelling events [74]. Nevertheless, sampling availability and the environmental conditions associated with the selected days also appear to have influenced validation performance, although their individual contributions cannot be isolated. MUR continued to show substantial errors under L3-sampled conditions and remained the weakest-performing product after the upwelling event was excluded, consistent with limitations in its representation of rapidly evolving coastal SST variability.

An additional source of discrepancy between the satellite and in situ observations may arise from differences in the physical depth and SST definition represented by each dataset. Infrared satellite products measure skin SST at the ocean surface, whereas L4 products are designed to estimate foundation SST [1,3,17], while the Sailbuoy records bulk SST at approximately 1 m depth. These measurements therefore do not represent identical physical quantities, as near-surface vertical temperature gradients associated with the thermal skin layer and diurnal warming can cause differences between skin and bulk SST [1,73]. Skin-bulk temperature differences can exceed 2 °C [75,76], although their magnitude and direction depend on the prevailing atmospheric forcing and upper-ocean thermal structure. Consequently, these differences may contribute to systematic offsets between the satellite and Sailbuoy observations, but their contribution to satellite–Sailbuoy discrepancies is unlikely to remain constant throughout the surveys. The mean Sailbuoy diurnal SST cycle had a range of 0.34 °C in 2024 and 0.44 °C in 2025, suggesting that diurnal warming was present during both surveys and may contribute to discrepancies between satellite and Sailbuoy SST at daily timescales. This may be particularly relevant during the austral summer conditions sampled in 2025, when strong surface heating and wind-driven upwelling could influence near-surface temperature gradients and the upper-ocean vertical structure along the southeast coast of South Africa [77,78].

Spatial and temporal sampling differences may also introduce uncertainty to the satellite-in situ comparisons. Satellite SST values were matched to individual Sailbuoy observations before daily averaging. However, the moving platform sampled changing locations and potentially distinct water masses. Differences in the spatial representation of fronts, SST gradients, as well as observation timing and spatial resolution, may contribute to observed mismatches [79]. The daily SST range comparisons provide additional context

for interpreting these differences: when satellite SST values fall within the range recorded by the Sailbuoy on a given day, their difference from the daily mean may partly reflect natural spatial and temporal variability rather than satellite-product error alone. However, falling within this range does not establish that a satellite value accurately represents SST at the corresponding location and time. The respective contributions of satellite-product error, depth-related SST differences, and spatial and temporal representativeness cannot be isolated using the present analysis. Furthermore, the limited number of daily matchups, particularly during the 2025 survey, and the smaller sample sizes in the sensitivity analysis limit the strength of comparisons between products. These uncertainties should be considered when interpreting validation statistics, particularly during periods of strong atmospheric forcing and rapidly evolving coastal conditions.

5. Implications and Future Applications

Satellite-derived SST products remain valuable observational tools for monitoring coastal ocean variability and supporting a range of scientific and operational applications, including ocean and climate research, ecosystem studies, numerical model evaluation and forecasting, and fisheries and other marine management activities [30]. Their broad spatial coverage is particularly valuable in coastal regions where sustained in situ observations are limited, allowing broader thermal structure to be characterised across spatial scales that cannot be sampled continuously by autonomous platforms alone. The results of this study provide practical guidance for the use of satellite SST products in dynamic coastal environments. Under relatively stable and cloud-free conditions, the products examined here provided reliable representations of coastal SST variability and may be appropriate for many regional applications. However, sparse infrared observations should not necessarily be interpreted as representative of the full range of coastal conditions. During rapidly evolving upwelling events accompanied by extensive cloud cover, particular caution is warranted, as data gaps resulted in the most extreme SST conditions being missed. Gap-filled L4 products provide valuable spatial and temporal continuity under these conditions, but complete coverage should not be interpreted as evidence that the magnitude or timing of rapidly evolving coastal temperature changes has been accurately resolved. Product performance should therefore be interpreted in the context of prevailing environmental conditions and the spatial and temporal scales of interest. Spatial resolution, temporal sampling, processing level, and data availability should also be considered, with concurrent in situ observations used where possible when resolving short-term or fine-scale variability.

An important outcome of this study is the value of autonomous platforms such as Sailbuoys for validating satellite-derived SST products in highly dynamic coastal environments. While moving platforms sample evolving water masses and therefore introduce potential representativeness differences relative to fixed-point observations, they provide spatially extensive in situ measurements across heterogeneous ocean conditions that are difficult to capture otherwise [42]. The observation that most satellite SST products frequently remained within the daily Sailbuoy SST envelope further indicates that some apparent satellite-in situ differences may reflect natural short-term variability rather than retrieval error alone, reinforcing the importance of accounting for sub-daily variability in coastal validation studies. Together, these results highlight the complementary nature of satellite and Sailbuoy observations, combining spatial coverage beyond the Sailbuoy sampling footprint. This enables their combined use in applications requiring both local in situ accuracy and synoptic-scale coverage.

Despite the increasing use of satellite SST products globally, relatively few studies have examined their performance in southern African waters, particularly under contrasting coastal regimes characterised by strong frontal activity and episodic upwelling. Previous

assessments have largely focused on global-scale validation or selected boundary current systems [14,27,34,71], with fewer multi-product intercomparisons available for the Agulhas Current region [40,66,80,81]. This study therefore provides a regional benchmark for satellite SST performance under contrasting coastal conditions in the Agulhas Current region. Future work should extend these comparisons across additional seasons and a wider range of oceanographic conditions, particularly during extreme events and periods of enhanced mesoscale and submesoscale variability. Further integration of autonomous platforms, moored time series, and satellite observations would improve constraints of SST uncertainty in coastal regions and support the development of more robust monitoring strategies for the Agulhas Current system [3,55].

6. Conclusions

Satellite SST product performance differed between the two surveys conducted along the inshore boundary of the Agulhas Current, which sampled contrasting coastal conditions. During the 2024 survey, all products successfully resolved the dominant thermal structure with high agreement against Sailbuoy observations. In contrast, satellite product performance was poorer during the 2025 survey, which coincided with a wind-driven upwelling event characterised by rapid thermal variability, strong spatial gradients, and reduced infrared sampling under persistent cloud cover. Differences between products further indicate that retrieval performance is not solely governed by environmental forcing, but also by sensor design, retrieval strategy, and compositing methodology. Sentinel-3 provided the most consistent representation of SST variability across both deployments, while OSTIA delivered the most stable gap-free fields. L3 products (MODIS and VIIRS) showed reduced ability to capture rapid coastal cooling, reflecting limitations associated with compositing and reduced temporal representativeness during highly dynamic conditions. These results highlight the importance of matching product choice to the dominant oceanographic regime and application requirements, particularly in highly dynamic western boundary current systems where variability occurs at scales close to or below the effective resolution of satellite observations.

Author Contributions: Conceptualisation, N.R., T.M., J.H., S.S. and M.D.P.; methodology, N.R., T.M., J.H., S.S. and M.D.P.; investigation, N.R.; formal analysis, N.R.; data curation, N.R.; writing—original draft preparation, N.R.; writing—review and editing, T.M., J.H., S.S. and M.D.P.; supervision, T.M., J.H., S.S. and M.D.P.; project administration, T.M. and J.H. All authors have read and agreed to the published version of the manuscript.

Funding: This research is funded by the Research Infrastructure Professional Programme (RIPP2409 09267367), a funding and capacity-building initiative by the National Research Foundation (NRF) and the South African Environmental Observation Network (SAEON). The Sailbuoy deployments were facilitated and funded by the University of Gothenburg through the Wallenberg Academy Fellowship of S.S. (WAF 2015.0186). S.S. and M.D.P. have received funding from the European Union's Horizon Europe ERC Synergy Grant programme under grant agreement No. 101118693 (WHIRLS).

Data Availability Statement: All satellite datasets used in this study are publicly available from their respective data providers. The Sailbuoy in situ observations used in this study is available online (Zenodo: https://doi.org/10.5281/zenodo.22792862).

Acknowledgments: The South African Environmental Observation Network (SAEON) Egagasini Node provided administrative support and research facilities. We thank Sea Technology Services (STS) for Sailbuoy maintenance and technical support, and the University of Gothenburg for piloting the Sailbuoy. We acknowledge the crew of the RV Observer (NRF-SAIAB), particularly Captain Koos Smith, for assistance with Sailbuoy deployment and recovery. The Sailbuoy deployments were conducted during the African Coelacanth Ecosystem Programme (ACEP) project. We would also like

thank the three anonymous reviewers for their time and valuable suggestions, which helped improve the manuscript.

Conflicts of Interest: The authors declare no conflicts of interest. The funders had no role in the design of the study; in the collection, analyses, or interpretation of data; in the writing of the manuscript; or in the decision to publish the results.

Abbreviations

The following abbreviations are used in this manuscript:

L2	Level 2
L3	Level 3
L4	Level 4
MODIS	Moderate Resolution Imaging Spectroradiometer
MUR	Multi-scale Ultra-high Resolution
OSTIA	Operational Sea Surface Temperature and Ice Analysis
RMSE	Root Mean Square Error
SLSTR	Sea and Land Surface Temperature Radiometer
SST	Sea Surface Temperature
USV	Uncrewed Surface Vehicles
VIIRS	Visible Infrared Imaging Radiometer Suite

References

1. Minnett, P.J.; Alvera-Azcárate, A.; Chin, T.M.; Corlett, G.K.; Gentemann, C.L.; Karagali, I.; Li, X.; Marsouin, A.; Marullo, S.; Maturi, E.; et al. Half a century of satellite remote sensing of sea-surface temperature. *Remote Sens. Environ.* **2019**, *233*, 111366. [CrossRef]
2. Yu, Y.; Zhang, H.-R.; Jin, J.; Wang, Y. Trends of sea surface temperature and sea surface temperature fronts in the South China Sea during 2003–2017. *Acta Oceanol. Sin.* **2019**, *38*, 106–115. [CrossRef]
3. Donlon, C.; Robinson, I.; Casey, K.S.; Vazquez-Cuervo, J.; Armstrong, E.; Arino, O.; Gentemann, C.; May, D.; LeBorgne, P.; Piollé, J.; et al. The Global Ocean Data Assimilation Experiment High-resolution Sea Surface Temperature Pilot Project. *Bull. Am. Meteorol. Soc.* **2007**, *88*, 1197–1214. [CrossRef]
4. Ghani, M.H.; Hole, L.R.; Fer, I.; Kourafalou, V.H.; Wienders, N.; Kang, H.; Drushka, K.; Peddie, D. The SailBuoy remotely-controlled unmanned vessel: Measurements of near surface temperature, salinity and oxygen concentration in the Northern Gulf of Mexico. *Methods Oceanogr.* **2014**, *10*, 104–121. [CrossRef]
5. Schmitt, R. The Ocean's Role in Climate. *Oceanography* **2018**, *31*, 32–40. [CrossRef]
6. Falkowski, P.G.; Ziemann, D.; Kolber, Z.; Bienfang, P.K. Role of eddy pumping in enhancing primary production in the ocean. *Nature* **1991**, *352*, 55–58. [CrossRef]
7. Van Niekerk, L.; Lamberth, S.J.; James, N.C.; Taljaard, S.; Adams, J.B.; Theron, A.K.; Krug, M. The Vulnerability of South African Estuaries to Climate Change: A Review and Synthesis. *Diversity* **2022**, *14*, 697. [CrossRef]
8. Vazquez-Cuervo, J.; García-Reyes, M.; Wethey, D.S.; Ciani, D.; Gomez-Valdes, J. Application and Comparison of Satellite-Derived Sea Surface Temperature Gradients to Identify Seasonal and Interannual Variability off the California Coast: Preliminary Results and Future Perspectives. *Remote Sens.* **2025**, *17*, 2722. [CrossRef]
9. Quartly, G.D.; Srokosz, M.A. SST observations of the Agulhas and East Madagascar retroflections by the TRMM Microwave Imager. *J. Phys. Oceanogr.* **2002**, *32*, 1585–1592. [CrossRef]
10. Zhang, Z.; Miao, M.; Qiu, B.; Tian, J.; Jing, Z.; Chen, G.; Chen, Z.; Zhao, W. Submesoscale Eddies Detected by SWOT and Moored Observations in the Northwestern Pacific. *Geophys. Res. Lett.* **2024**, *51*, e2024GL110000. [CrossRef]
11. Lutjeharms, J.R. The coastal oceans of south-eastern Africa (15, W). *Sea* **2006**, *14*, 783–834.
12. Leber, G.M.; Beal, L.M.; Elipot, S. Wind and current forcing combine to drive strong upwelling in the Agulhas Current. *J. Phys. Oceanogr.* **2017**, *47*, 123–134. [CrossRef]
13. Merchant, C.J.; Embury, O.; Bulgin, C.E.; Block, T.; Corlett, G.K.; Fiedler, E.; Good, S.A.; Mittaz, J.; Rayner, N.A.; Berry, D.; et al. Satellite-based time-series of sea-surface temperature since 1981 for climate applications. *Sci. Data* **2019**, *6*, 223. [CrossRef] [PubMed]
14. Koutantou, K.; Brunner, P.; Vazquez-Cuervo, J. Validation of NASA Sea Surface Temperature Satellite Products Using Saildrone Data. *Remote Sens.* **2023**, *15*, 2277. [CrossRef]
15. Kent, E.C.; Kennedy, J.J. Historical Estimates of Surface Marine Temperatures. *Annu. Rev. Mar. Sci.* **2021**, *13*, 283–311. [CrossRef] [PubMed]

16. Chelton, D.B.; Wentz, F.J. Global Microwave Satellite Observations of Sea Surface Temperature for Numerical Weather Prediction and Climate Research. *Bull. Am. Meteorol. Soc.* **2005**, *86*, 1097–1116. [CrossRef]
17. Donlon, C.J.; Martin, M.; Stark, J.; Roberts-Jones, J.; Fiedler, E.; Wimmer, W. The Operational Sea Surface Temperature and Sea Ice Analysis (OSTIA) system. *Remote Sens. Environ.* **2012**, *116*, 140–158. [CrossRef]
18. Chin, T.M.; Vazquez-Cuervo, J.; Armstrong, E.M. A multi-scale high-resolution analysis of global sea surface temperature. *Remote Sens. Environ.* **2017**, *200*, 154–169. [CrossRef]
19. Hunt, S.E.; Mittaz, J.P.D.; Smith, D.; Polehampton, E.; Yemelyanova, R.; Woolliams, E.R.; Donlon, C. Comparison of the Sentinel-3A and B SLSTR Tandem Phase Data Using Metrological Principles. *Remote Sens.* **2020**, *12*, 2893. [CrossRef]
20. Donlon, C.J.; Minnett, P.J.; Gentemann, C.; Nightingale, T.J.; Barton, I.J.; Ward, B.; Murray, M.J. Toward improved validation of satellite sea surface skin temperature measurements for climate research. *J. Clim.* **2002**, *15*, 353–369. [CrossRef]
21. Jia, C.; Minnett, P.J.; Szczodrak, M. Assessment of Accuracy of Moderate-Resolution Imaging Spectroradiometer Sea Surface Temperature at High Latitudes Using Saildrone Data. *Remote Sens.* **2024**, *16*, 2008. [CrossRef]
22. Emery, W.J.; Yu, Y.; Wick, G.A.; Schluessel, P.; Reynolds, R.W. Correcting infrared satellite estimates of sea surface temperature for atmospheric water vapor attenuation. *J. Geophys. Res. Ocean.* **1994**, *99*, 5219–5236. [CrossRef]
23. Rouault, M.; Florenchie, P.; Fauchereau, N.; Reason, C.J.C. South East tropical Atlantic warm events and southern African rainfall. *Geophys. Res. Lett.* **2003**, *30*, 8009. [CrossRef]
24. Wentz, F.J.; Gentemann, C.; Smith, D.; Chelton, D. Satellite Measurements of Sea Surface Temperature Through Clouds. *Science* **2000**, *288*, 847–850. [CrossRef] [PubMed]
25. Robinson, I.S. *Measuring the Oceans from Space: The Principles and Methods of Satellite Oceanography*; Springer: Berlin, Germany, 2004.
26. Merchant, C.J.; Embury, O.; Roberts-Jones, J.; Fiedler, E.; Bulgin, C.E.; Corlett, G.K.; Good, S.; McLaren, A.; Rayner, N.; Morak-Bozzo, S.; et al. Sea surface temperature datasets for climate applications from Phase 1 of the European Space Agency Climate Change Initiative (SST CCI). *Geosci. Data J.* **2014**, *1*, 179–191. [CrossRef]
27. Reynolds, R.W.; Chelton, D.B. Comparisons of daily sea surface temperature analyses for 2007–08. *J. Clim.* **2010**, *23*, 3545–3562. [CrossRef]
28. Reynolds, R.W.; Chelton, D.B.; Roberts-Jones, J.; Martin, M.J.; Menemenlis, D.; Merchant, C.J. Objective determination of feature resolution in two sea surface temperature analyses. *J. Clim.* **2013**, *26*, 2514–2533. [CrossRef]
29. Jia, C.; Minnett, P.J. Ocean Warm Skin Signals Observed by Saildrone at High Latitudes. *Geophys. Res. Lett.* **2023**, *50*, e2022GL102384. [CrossRef]
30. O'Carroll, A.G.; Armstrong, E.M.; Beggs, H.M.; Bouali, M.; Casey, K.S.; Corlett, G.K.; Dash, P.; Donlon, C.J.; Gentemann, C.L.; Høyer, J.L.; et al. Observational Needs of Sea Surface Temperature. *Front. Mar. Sci.* **2019**, *6*, 420. [CrossRef]
31. Lee, E.-Y.; Park, K.-A. Validation of Satellite Sea Surface Temperatures and Long-Term Trends in Korean Coastal Regions over Past Decades (1982–2018). *Remote Sens.* **2020**, *12*, 3742. [CrossRef]
32. Ahmed, A.; Fox-Kemper, B.; Watkins, D.M.; Wexler, D.; Wilhelmus, M.M. Estuarine temperature variability: Integrating four decades of remote sensing observations and in-situ sea surface measurements. *Remote Sens. Environ.* **2025**, *322*, 114643. [CrossRef]
33. Richardson, P.L. Drifters and floats. In *Elements of Physical Oceanography: A Derivative of the Encyclopedia of Ocean Sciences*; Thorpe, S.A., Ed.; Academic Press: Cambridge, MA, USA, 2009; pp. 89–96.
34. Vazquez-Cuervo, J.; Gomez-Valdes, J.; Bouali, M.; Miranda, L.E.; der Stocken, T.V.; Tang, W.; Gentemann, C. Using Saildrones to Validate Satellite-Derived Sea Surface Salinity and Sea Surface Temperature along the California/Baja Coast. *Remote Sens.* **2019**, *11*, 1964. [CrossRef]
35. Gentemann, C.L.; Scott, J.P.; Mazzini, P.L.F.; Pianca, C.; Akella, S.; Minnett, P.J.; Cornillon, P.; Fox-Kemper, B.; Cetinić, I.; Chin, T.M.; et al. Saildrone: Adaptively Sampling the Marine Environment. *Bull. Am. Meteorol. Soc.* **2020**, *101*, E744–E762. [CrossRef]
36. Beal, L.M.; Elipot, S. Broadening not strengthening of the Agulhas Current since the early 1990s. *Nature* **2016**, *540*, 570–573. [CrossRef] [PubMed]
37. Malan, N.; Backeberg, B.; Biastoch, A.; Durgadoo, J.V.; Samuelsen, A.; Reason, C.; Hermes, J. Agulhas Current Meanders Facilitate Shelf-Slope Exchange on the Eastern Agulhas Bank. *J. Geophys. Res. Ocean.* **2018**, *123*, 4762–4778. [CrossRef]
38. Tedesco, P.; Gula, J.; Ménesguen, C.; Penven, P.; Krug, M. Generation of Submesoscale Frontal Eddies in the Agulhas Current. *J. Geophys. Res. Ocean.* **2019**, *124*, 7606–7625. [CrossRef]
39. Goschen, W.S.; Bornman, T.G.; Deyzel, S.H.P.; Schumann, E.H. Coastal upwelling on the far eastern Agulhas Bank associated with large meanders in the Agulhas Current. *Cont. Shelf Res.* **2015**, *101*, 34–46. [CrossRef]
40. Carr, M.; Lamont, T.; Krug, M. Satellite Sea Surface Temperature Product Comparison for the Southern African Marine Region. *Remote Sens.* **2021**, *13*, 1244. [CrossRef]
41. Smit, A.J.; Roberts, M.; Anderson, R.J.; Dufois, F.; Dudley, S.F.J.; Bornman, T.G.; Olbers, J.; Bolton, J.J. A Coastal Seawater Temperature Dataset for Biogeographical Studies: Large Biases between In Situ and Remotely-Sensed Data Sets around the Coast of South Africa. *PLoS ONE* **2013**, *8*, e81944. [CrossRef] [PubMed]

42. Patterson, R.G.; Cronin, M.F.; Swart, S.; Beja, J.; Edholm, J.M.; McKenna, J.; Palter, J.B.; Parker, A.; Addey, C.I.; Boone, W.; et al. Uncrewed surface vehicles in the Global Ocean Observing System: A new frontier for observing and monitoring at the air-sea interface. *Front. Mar. Sci.* **2025**, *12*, 1523585. [CrossRef]
43. Swart, S.; du Plessis, M.D.; Thompson, A.F.; Biddle, L.C.; Giddy, I.; Linders, T.; Mohrmann, M.; Nicholson, S.-A. Submesoscale Fronts in the Antarctic Marginal Ice Zone and Their Response to Wind Forcing. *Geophys. Res. Lett.* **2020**, *47*, e2019GL086649. [CrossRef]
44. Castro, S.L.; Emery, W.J.; Wick, G.A.; Tandy, W. Submesoscale Sea Surface Temperature Variability from UAV and Satellite Measurements. *Remote Sens.* **2017**, *9*, 1089. [CrossRef]
45. Schmidt, K.M.; Swart, S.; Reason, C.; Nicholson, S.A. Evaluation of satellite and reanalysis wind products with in situ wave glider wind observations in the Southern Ocean. *J. Atmos. Ocean. Technol.* **2017**, *34*, 2551–2568. [CrossRef]
46. Villareal, T.A.; Wilson, C. A Comparison of the Pac-X Trans-Pacific Wave Glider Data and Satellite Data (MODIS, Aquarius, TRMM and VIIRS). *PLoS ONE* **2014**, *9*, e92280. [CrossRef] [PubMed]
47. Zhang, D.; Cronin, M.F.; Meinig, C.; Farrar, J.T.; Jenkins, R.; Peacock, D.; Keene, J.; Sutton, A.; Yang, Q. Comparing Air-Sea Flux Measurements from a New Unmanned Surface Vehicle and Proven Platforms During the Spurs-2 Field Campaign. *Oceanography* **2019**, *32*, 122–133. [CrossRef]
48. Offshore Sensing AS. Sailbuoy. Available online: https://sailbuoy.no/ (accessed on 5 March 2026).
49. Wullenweber, N.; Hole, L.; Ghaffari, P.; Graves, I.; Tholo, H.; Camus, L. SailBuoy Ocean Currents: Low-Cost Upper-Layer Ocean Current Measurements. *Sensors* **2022**, *22*, 5553. [CrossRef]
50. Data Store. EUMETSAT, 2017. Available online: https://data.eumetsat.int/product/ (accessed on 12 November 2025).
51. Bonekamp, H.; Montagner, F.; Santacesaria, V.; Nogueira Loddo, C.; Wannop, S.; Tomazic, I.; O'Carroll, A.; Kwiatkowska, E.; Scharroo, R.; Wilson, H. Core operational Sentinel-3 marine data product services as part of the Copernicus Space Component. *Ocean. Sci.* **2016**, *12*, 787–795. [CrossRef]
52. NASA. MODIS and VIIRS Sea Surface Temperature Data. Available online: https://oceandata.sci.gsfc.nasa.gov/ (accessed on 18 February 2026).
53. Saleh, A.K.; Al-Anzi, B.S. Statistical Validation of MODIS-Based Sea Surface Temperature in Shallow Semi-Enclosed Marginal Sea: A Comparison between Direct Matchup and Triple Collocation. *Water* **2021**, *13*, 1078. [CrossRef]
54. Marine.copernicus.eu. CMEMS Home, 2025. Available online: https://marine.copernicus.eu/ (accessed on 12 July 2025).
55. Good, S.; Fiedler, E.; Mao, C.; Martin, M.J.; Maycock, A.; Reid, R.; Roberts-Jones, J.; Searle, T.; Waters, J.; While, J.; et al. The Current Configuration of the OSTIA System for Operational Production of Foundation Sea Surface Temperature and Ice Concentration Analyses. *Remote Sens.* **2020**, *12*, 720. [CrossRef]
56. Worsfold, M.; Good, S.; Atkinson, C.; Embury, O. Presenting a Long-Term, Reprocessed Dataset of Global Sea Surface Temperature Produced Using the OSTIA System. *Remote Sens.* **2024**, *16*, 3358. [CrossRef]
57. Cronin, M.F.; Zhang, D.; Wills, S.M.; Reeves Eyre, J.E.J.; Thompson, L.; Anderson, N. Diurnal warming rectification in the tropical Pacific linked to sea surface temperature front. *Nat. Geosci.* **2024**, *17*, 316–322. [CrossRef]
58. Pyper, B.J.; Peterman, R.M. Comparison of methods to account for autocorrelation in correlation analyses of fish data. *Can. J. Fish. Aquat. Sci.* **1998**, *55*, 2127–2140. [CrossRef]
59. Beal, L.M.; Elipot, S.; Houk, A.; Leber, G.M. Capturing the transport variability of a western boundary jet: Results from the Agulhas Current Time-Series Experiment (ACT). *J. Phys. Oceanogr.* **2015**, *45*, 1302–1324. [CrossRef]
60. Krug, M.; Swart, S.; Gula, J. Submesoscale cyclones in the Agulhas current. *Geophys. Res. Lett.* **2017**, *44*, 346–354. [CrossRef]
61. Lamont, T.; Halo, I.; Russo, C.S. Impacts of Agulhas Current meanders on intermediate water masses along the adjacent continental slope and shelf. *Cont. Shelf Res.* **2024**, *274*, 105197. [CrossRef]
62. Hancke, L.; Roberts, M.J.; Smeed, D.; Jebri, F. Cold ridge formation mechanisms on the Agulhas Bank (South Africa) as revealed by satellite-tracked drifters. *Deep. Sea Res. Part II Top. Stud. Oceanogr.* **2023**, *208*, 105245. [CrossRef]
63. Jury, M.R. Wind Vorticity and Upwelling along the Coast of South Africa. *Coasts* **2024**, *4*, 619–637. [CrossRef]
64. Emery, W.J.; Castro, S.; Wick, G.A.; Schluessel, P.; Donlon, C. Estimating Sea Surface Temperature from Infrared Satellite and In Situ Temperature Data. *Bull. Am. Meteorol. Soc.* **2001**, *82*, 2773–2785. [CrossRef]
65. Robinson, I.S. The methods of satellite oceanography. In *Discovering the Ocean from Space: The Unique Applications of Satellite Oceanography*; Springer: Berlin/Heidelberg, Germany, 2010; pp. 7–67.
66. Meneghesso, C.; Seabra, R.; Broitman, B.R.; Wethey, D.S.; Burrows, M.T.; Chan, B.K.; Guy-Haim, T.; Ribeiro, P.A.; Rilov, G.; Santos, A.M.; et al. Remotely-sensed L4 SST underestimates the thermal fingerprint of coastal upwelling. *Remote Sens. Environ.* **2020**, *237*, 111588. [CrossRef]
67. Vazquez-Cuervo, J.; Dewitte, B.; Chin, T.M.; Armstrong, E.M.; Purca, S.; Alburqueque, E. An analysis of SST gradients off the Peruvian Coast: The impact of going to higher resolution. *Remote Sens. Environ.* **2013**, *131*, 76–84. [CrossRef]

68. Bulgin, C.E.; Faulkner, A.; Merchant, C.J.; Corlett, G.K.; McCarroll, N.; Embury, O.; Polehampton, E.; McGurk, C. Improving the combined use of reflectance and thermal channels for ocean and coastal cloud detection for the Sea and Land Surface Temperature Radiometer (SLSTR). *Remote Sens. Environ.* **2023**, *290*, 113531. [CrossRef]
69. Mao, C.; Good, S.; Worsfold, M. Use of SLSTR Sea Surface Temperature Data in OSTIA as a Reference Sensor: Implementation and Validation. *Remote Sens.* **2024**, *16*, 3396. [CrossRef]
70. Schlegel, R.W.; Oliver, E.C.J.; Wernberg, T.; Smit, A.J. Nearshore and Offshore Co-Occurrence of Marine Heatwaves and Cold-Spells. *Prog. Oceanogr.* **2017**, *151*, 189–205. [CrossRef]
71. Martin, M.; Dash, P.; Ignatov, A.; Banzon, V.; Beggs, H.; Brasnett, B.; Cayula, J.F.; Cummings, J.; Donlon, C.; Gentemann, C.; et al. Group for High Resolution Sea Surface Temperature (GHRSST) Analysis Fields Inter-Comparisons. Part 1: A GHRSST Multi-Product Ensemble (GMPE). *Deep Res. Part II Top. Stud. Oceanogr.* **2012**, *77–80*, 21–30.
72. Schloesser, F.; Cornillon, P.; Donohue, K.; Boussidi, B.; Iskin, E. Evaluation of Thermosalinograph and VIIRS Data for the Characterization of Near-Surface Temperature Fields. *J. Atmos. Ocean. Technol.* **2016**, *33*, 1843–1858. [CrossRef]
73. Kawai, Y.; Wada, A. Diurnal Sea Surface Temperature Variation and Its Impact on the Atmosphere and Ocean: A Review. *J. Oceanogr.* **2007**, *63*, 721–744. [CrossRef]
74. Huang, B.; Yin, X.; Carton, J.A.; Chen, L.; Graham, G.; Liu, C.; Smith, T.; Zhang, H.-M. Understanding Differences in Sea Surface Temperature Intercomparisons. *J. Atmos. Ocean. Technol.* **2023**, *40*, 455–473. [CrossRef]
75. Alappattu, D.P.; Wang, Q.; Yamaguchi, R.; Lind, R.J.; Reynolds, M.; Christman, A.J. Warm layer and cool skin corrections for bulk water temperature measurements for air-sea interaction studies. *J. Geophys. Res. Ocean.* **2017**, *122*, 6470–6481. [CrossRef]
76. Al-Shehhi, M.R. Uncertainty in satellite sea surface temperature with respect to air temperature, dust level, wind speed and solar position. *Reg. Stud. Mar. Sci.* **2022**, *53*, 102385. [CrossRef]
77. Schumann, E.H.; Cohen, A.L.; Jury, M.R. Coastal sea surface temperature variability along the south coast of South Africa and the relationship to regional and global climate. *J. Mar. Res.* **1995**, *53*.
78. Goschen, W.; Schumann, E.; Bernard, K.; Bailey, S.; Deyzel, S. Upwelling and Ocean Structures off Algoa Bay and the South-East Coast of South Africa. *Afr. J. Mar. Sci.* **2012**, *34*, 525–536. [CrossRef]
79. Gentemann, C.L. Three way validation of MODIS and AMSR-E sea surface temperatures. *J. Geophys. Res. Ocean.* **2014**, *119*, 2583–2598. [CrossRef]
80. Rouault, M.; Penven, P.; Pohl, B. Warming in the Agulhas Current System since the 1980's. *Geophys. Res. Lett.* **2009**, *36*, L12602. [CrossRef]
81. Russo, C.S.; Veitch, J.; Carr, M.; Fearon, G.; Whittle, C. An Intercomparison of Global Reanalysis Products for Southern Africa's Major Oceanographic Features. *Front. Mar. Sci.* **2022**, *9*, 837906. [CrossRef]

Disclaimer/Publisher's Note: The statements, opinions and data contained in all publications are solely those of the individual author(s) and contributor(s) and not of MDPI and/or the editor(s). MDPI and/or the editor(s) disclaim responsibility for any injury to people or property resulting from any ideas, methods, instructions or products referred to in the content.